



1 **The Tibetan Plateau Space-based**
2 **Tropospheric Aerosol Climatology: 2007–**
3 **2020**

4 Honglin Pan^{1,2}, Jianping Huang^{1*}, Jiming Li¹, Zhongwei Huang¹,
5 Tian Zhou¹, Kanike Raghavendra Kumar³

6
7
8
9
10 ¹*Collaborative Innovation Center for Western Ecological Safety, College of*
11 *Atmospheric Sciences, Lanzhou University, Lanzhou, 730000, China*

12 ²*Institute of Desert Meteorology, China Meteorological Administration, National*
13 *Observation and Research Station of Desert Meteorology, Taklimakan Desert of*
14 *Xinjiang, Taklimakan Desert Meteorology Field Experiment Station of China*
15 *Meteorological Administration, Xinjiang Key Laboratory of Desert Meteorology and*
16 *Sandstorm, Key Laboratory of Tree-ring Physical and Chemical Research, China*
17 *Meteorological Administration, Urumqi, 830002, Xinjiang, China*

18 ³*Department of Engineering Physics, College of Engineering, Koneru Lakshmaiah*
19 *Education Foundation, Vaddeswaram, Guntur 522302, Andhra Pradesh, India*

20
21
22
23
24
25
26 Correspondence: Jianping Huang (hjp@lzu.edu.cn)

27
28
29
30
31
32
33



34 **Abstract.** A comprehensive and robust dataset of tropospheric aerosol properties is
35 important for understanding the effects of aerosol-radiation feedback on the climate
36 system and reducing the uncertainties of climate models. The third pole of Earth
37 (Tibetan Plateau, TP) is highly challenging to obtain long-term in situ aerosol data due
38 to its harsh environmental conditions. Here, we provide more reliable the new vertical
39 aerosol index (AI) parameter from the spaceborne-based Lidar (CALIOP) of CALIPSO
40 over TP during 2007-2020 between daytime and nighttime to investigate the aerosol's
41 climatology. The calculated vertical AI was derived from the aerosol extinction
42 coefficient (EC), which was rigorously quality-checked and validation, strictly quality
43 checked, and validated for passive satellite sensors (MODIS) and ground-based LIDAR
44 measurements. Generally, all those facts demonstrate the agreement of the AI dataset
45 with the CALIOP and ground-based LIDAR. Besides, all the evidence shows that after
46 removing the low-reliability aerosol target signal, the optimized data can obtain the
47 aerosol characteristics with higher reliability. Our data set also reveals the patterns and
48 numbers of high-altitude vertical structure characteristics of the aerosol troposphere
49 over the TP. Our dataset will help to update and makeup the observational aerosol data
50 in the TP. We encourage climate modeling groups to consider new analyses of the AI
51 vertical patterns, comparing the recovered datasets, with the potential to increase our
52 understanding of the aerosol-cloud-radiation-precipitation interaction and its climate
53 effects. Data described in this work are available at
54 <https://data.tpdc.ac.cn/en/disallow/03fa38bc-25bd-46c5-b8ce-11b457f7d7fd>
55 DOI:10.11888/Atmos.tpdc.300614. (Honglin Pan et al., 2023).

56
57 **Keywords:** Tibetan Plateau, Aerosol index vertical structure, Tropospheric aerosols,
58 Higher reliability, Aerosol climatology

59
60
61



62 **1 Introduction**

63 The three poles (i.e., the Arctic, Antarctic and Tibetan Plateau (TP)) have the
64 highest mountains in the world and store more snow, ice and fresh water than any other
65 place. The unique geographical location of the Antarctic, Arctic, and TP, as the unique
66 ecological, climatic, and natural environmental changes, have crucial role in global and
67 regional climate change. However, studies have found that these regions are susceptible
68 to climate change and that their differences may also affect key feedback loops for
69 global climate change and the sustainability of human societies. Unfortunately, our
70 understanding of the three poles, particularly the relations between the regions, remains
71 limited due to insufficient observation data. Currently, the collection of additional
72 research data for these extreme environments is one of the major bottlenecks in
73 facilitating comprehensive studies of these regions. Sufficient attention has been given
74 to the polar regions and the TP in successive IPCC reports (IPCC, 2013; 2021). The
75 similarities between TP and the other two polar regions are their low temperatures,
76 remote location, and large water storage capacity. On the other hand, TP has a more
77 highly complex climate than the Arctic and Antarctic (where ice is the primary medium)
78 and its land surface (including forests, grasslands, bare soil, lakes and glaciers) is more
79 diverse. These differences make the transport and accumulation of pollutants in the TP
80 region different from the other two polar regions.

81 The Tibetan Plateau (TP), is known as the "Third Pole" because it has the third
82 largest ice mass on Earth, after the Antarctic and Arctic regions (Qiu, 2008). TP is also
83 called the "Asia Water Towers", provides fresh water to 40% of the world's population
84 due to its vast water reserves such as glaciers, lakes and rivers (Immerzeel et al., 2010).
85 Furthermore, TP is the "Roof of the World", which covers an area of ~2.5 million km²
86 at an average altitude of about 4,000 m a.s.l. (above sea level) and includes all of Tibet
87 and parts of Qinghai, Gansu, Yunnan, and Sichuan in southwestern China, as well as
88 parts of India, Nepal, Bhutan, and Pakistan (Nieberding et al., 2020). To the north of
89 the TP region is situated by Taklamakan Desert (TD) (see Figure 1). This high altitude
90 and specific topographic area effectively serve as a heat source during the spring and



91 summer months. This thermal structure helps the TP to function virtually as an "air
92 pump", attracting warm and humid air from the lower latitude oceans by suction (Yanai
93 et al., 1992; Wu and Zhang, 1998; Wu et al., 2007; Wu et al., 2012). Consequently,
94 large-scale mountains play a crucial role in shaping regional and even global weather
95 and climate through mechanical and thermodynamic effects and affect the global
96 energy-water cycle (Xu et al., 2008; Molnar et al., 2010; Boos and Kuang, 2010; Wu et
97 al., 2015). It is closely related to the survival of human beings in the world.

98 Climate projections are simulated responses of the climate system to future
99 emission or concentration scenarios of greenhouse gases (GHGs) and aerosols and are
100 generally calculated using climate models. The reasons for the gap between models and
101 observations may also be due to inadequate solar, volcanic, and aerosol forcing used in
102 the models, and in some models, may be due to an overestimation of the response to
103 increasing GHG and other anthropogenic forcing (the latter reason includes mainly the
104 role of aerosols). The most significant uncertainties in predicting future climate change
105 are related to uncertainties in the distribution and properties of aerosols and clouds,
106 their interactions, and limitations in the representation of aerosols and clouds in global
107 climate models (IPCC, 2021). The primary aerosol type over the TP is dust, and its
108 spatiotemporal pattern is primarily contributed to the Taklimakan Desert (Liu et
109 al., 2008; Chen et al., 2013; 2022; Xu et al., 2015). Previously few studies of aerosol-
110 cloud-radiation-precipitation interaction have been conducted. For example, the dust
111 aerosols lifting over the TP reduce the radius of ice particles in the convective clouds
112 over the TP and prolong the cloud lifetime through the indirect radiation effect, which
113 can lead to the development of higher convective clouds. The dust-affected convective
114 clouds move further eastward under the action of westerly winds and merge with local
115 convective cloud masses, triggering heavy precipitation in the Yangtze River basin and
116 northern China downstream of the TP (Liu et al., JGR, 2019; Liu et al., NSR, 2019).
117 However, the effect of aerosol on the atmospheric energy and water cycle remains
118 uncertain, mainly due to lacking long-term and accurate vertical aerosol optical
119 properties dataset over the TP. This can help better understand aerosol's impact on the
120 atmospheric heating rate and stabilization and the subsequent cloud-precipitation



121 process. Therefore, constructing a more long-term and reliable vertically dataset of
122 aerosol optical parameters can make up the observational facts for aerosol-related study
123 and provide a scientific basis for improving the global climate model simulation over
124 the TP.

125 Generally, the primary aerosol optical characteristic parameters (such as extinction
126 coefficient (EC), aerosol optical depth (AOD)) acquisition method is in situ
127 observations, which have high precision. However, in situ observations are restricted
128 by the distribution of observation stations over TP. Hence, the resulting data lack spatial
129 continuity, making it difficult to use to meet the objectives of growing regional
130 atmospheric environmental studies (Chen et al.,2022; Goldberg et al.,2019; Giles et al.,
131 2019). Satellite remote sensing (active and passive) is an effective tool for collecting
132 aerosol optical information (including the vertical structure and spatial distribution)
133 over a wide range of spatial scales, significantly offsetting the deficiencies of in situ
134 observations. Satellite remote sensing can tackle difficulties connected to insufficient
135 data and uneven geographical distributions to a certain extent (Chen et al., 2022; Wei
136 et al.,2021). While for aerosol products from CALIPSO, the presence of some low-
137 reliability aerosol target (LRAT) caused by cloud contamination, solar noise
138 contamination, especially in the daytime, and ground clutter among mostly aerosol
139 observations skews the distribution of the aerosol EC toward larger values, at least some
140 of which may be identified as aerosols and retained in the analysis, makes the presence
141 of some low confidence aerosol targets bias the distribution of aerosol extinction in
142 most aerosol observations. The distribution of the aerosol EC will show greater biased
143 values (Thomason and Vernier, 2013; Kovilakam et al., 2020; Pan et al., 2020; Kahn et
144 al., 2010), and then will further enhance the aerosol index (AI) value due to the
145 influence of radiation transfer interaction between clouds and the absorption layer,
146 which will not truly reflect the differences in aerosol physical properties (Guan et al.,
147 2008; Liu et al., 2019; Kim et al.,2018). Hence, gaining high confidence in EC helps us
148 analyze aerosol optical properties and better lead to numerous pertinent uses of EC data,
149 is essential for accurately characterizing the upper range of aerosol ECs that occur on
150 the TP.



151 The present study provides a dataset of monthly average vertical structure
152 characteristics of tropospheric high confidence aerosol optical properties including
153 extinction coefficient (EC), aerosol optical depth (AOD), Angstrom exponent (AE),
154 aerosol index (AI) between the daytime and nighttime over the TP and surrounding
155 areas. The data for the above-mentioned optical properties were retrieved based on the
156 space-borne Lidar CALIOP data (Cloud-Aerosol Lidar with Orthogonal Polarization)
157 from Cloud-Aerosol Lidar and Infrared Pathfinder Satellite Observation (CALIPSO)
158 satellite for the period 2007-2020. The main objective of this study is to calculate new
159 and high-confidence aerosol optical parameter of AI in the vertical distribution, by the
160 strict quality control and validation for passive satellite sensor (MODIS) and ground-
161 based LIDAR. Since AI is dependent on aerosol concentration, optical properties and
162 altitude of the aerosol layer, and AI is particularly sensitive to high-altitude aerosols,
163 which is used to indicate small particles (those that act as cloud condensation nuclei)
164 with a high weight (Guan et al., 2010; Buchard et al., 2015; Liu et al., 2019; Nakajima
165 et al., 2001). The comprehensive data set of aerosol properties utilized in the study is
166 of substantial importance for understanding the impact of aerosol on the ecosystem and
167 reducing the uncertainties of climate models.

168 The data set in this study can more effectively characterize the vertical structure
169 of aerosols while following standardized quality control methods to obtain higher
170 confidence in the aerosol vertical structural properties covariate data sets, and allow for
171 comparison and application to the study of climate models and other atmospheric
172 science related problems between our record and with different data sets. To ensure
173 meaningful confidence estimates for the constructed aerosol covariates over the TP, it
174 is necessary to apply carefully the following correction procedures and analytical
175 validation. The main steps to construct the dataset are grouped as follows: (1) Removing
176 the low-confidence aerosol extinction coefficient for 532nm and 1064nm caused by the
177 misclassification of cloud and other interferences (e.g., surface clutter, hygroscopicity
178 etc.). Based on this, an interquartile range (IQR) method (see section 2.2) is utilized to
179 discard the low confidence targets, and further obtain the monthly average aerosol EC
180 for day and night with higher confidence; (2) the pseudo-Angstrom exponent (hereafter



181 AE) is calculated using the EC at 532 and 1064nm with higher confidence; (3) obtaining
182 vertical AI by the product of the AOD (the vertical integral of EC) and AE. (4)
183 Validation for the constructed AI with: MODIS and in situ LIDAR measurements using
184 standardized frequency distributions.

185 **2 The construction of the data set**

186 **2.1 Study area**

187 Figure 1 depicts the geopotential height of the TP and its surrounding areas (27-
188 42° N, 75-102° E, about 4,000 m a.s.l.), and schematic diagram of CALIPSO satellite
189 ground track over the TP in other months. The role of the "heat-driving air pump" of
190 the TP provides abundant water vapor for the formation of clouds (Luo et al., 1984;
191 Liou et al., 1986). Furthermore, the TP environment is greatly affected by natural and
192 anthropogenic aerosols from the surrounding regions (Chen et al., 2013; Bucci et
193 al., 2014; Xu et al., 2015). The strong convection generated by the TP will promote
194 aerosols' vertical transport and increase aerosols' content in the troposphere and
195 stratosphere (Vernier et al., 2015; Liu et al., 2022). Aerosols also serve as cloud
196 condensation nuclei (CCN) or ice nuclei (IN), modifying cloud structure properties and
197 precipitation (Twomey et al., 1977). Hence, the TP has been called the pumping pump
198 of water vapor, the clouds incubator, and the sand dust transfer station. By delivering
199 water vapor, clouds, and dust, it regulates extreme weather and climate in the
200 downstream and surrounding areas. It can be seen that the TP plays a crucial role in the
201 impact and regulation of global and regional climate or environments (Luo et al., 1984;
202 Rossow et al., 1999; Wan et al., 2017; Liu et al., 2022).

203

204

205

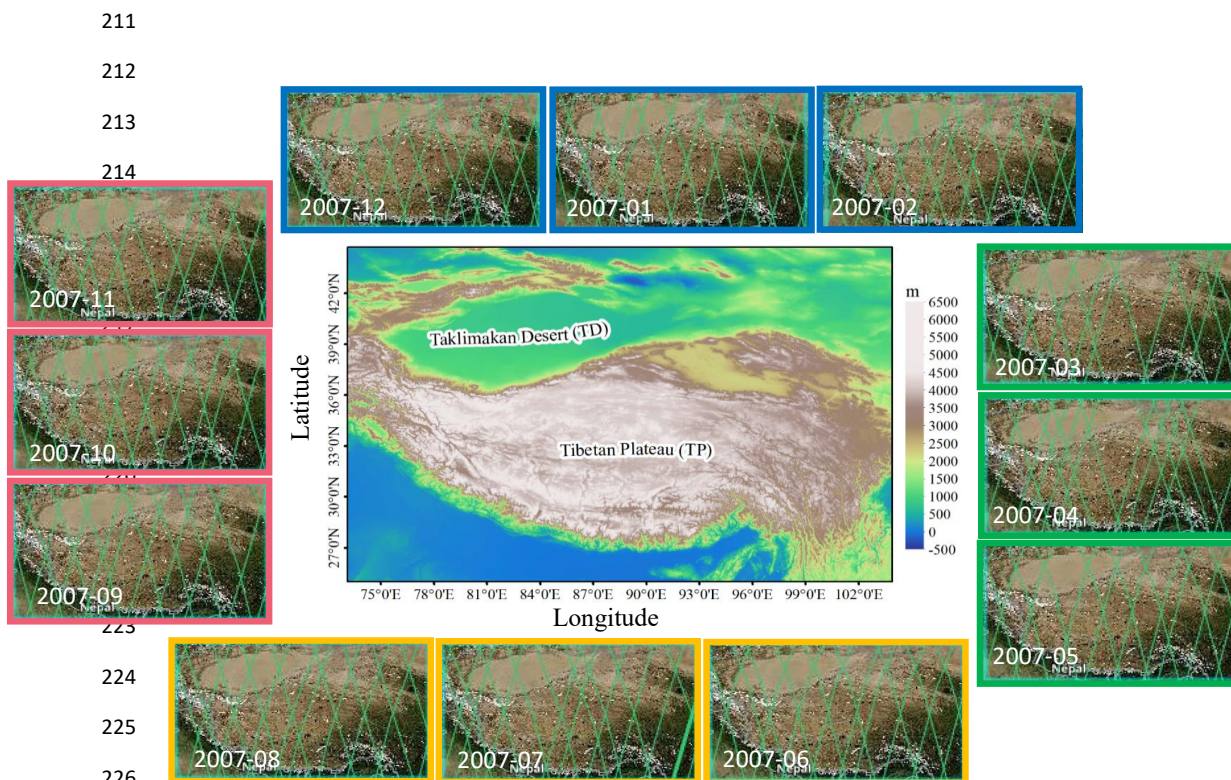
206

207

208

209

210



227 Figure. 1 The geopotential height of the TP and its surrounding areas (27-42°N,75-102°E),
228 schematic diagram of the transit of CALIPSO satellite orbits over the TP in other months (with 2007
229 as an example. March-May is spring, June-August is summer, September-November is autumn, and
230 December-February is winter).

231 2.2 CALIPSO-CALIOP data and low-reliability aerosol target (LRAT) clearing 232 method

233 CALIPSO (Cloud-Aerosol Lidar and Infrared Pathfinder Satellite Observations)
234 satellite was launched by NASA on 28 April 2006. The CALIOP (Cloud-Aerosol Lidar
235 with Orthogonal Polarization) onboard CALIPSO is the nadir-pointing dual-
236 wavelength polarization Lidar, which can provide the global and continuous
237 information on the vertical distribution of aerosols and clouds at 532 nm and 1064 nm
238 for daytime and nighttime. (Winker et al., 2007 and 2009). The CALIPSO-CALIOP
239 (version 4.20) level-2 aerosol profile product is selected in this study, with vertical and
240 horizontal resolutions of 60 m and 5 km, respectively. The used parameter includes



241 Extinction_Coefficient_532 and Extinction_Coefficient_1064 between daytime and
242 nighttime from 2007 to 2020. It should be noted that CALIOP observation data uses as
243 few instruments as necessary to complete the monthly aerosol climatology. We make
244 this decision to limit the impact of differences between instruments due to measurement
245 techniques and wavelength range as well as assess the general quality of the
246 instrument's data set.

247 The presence of some low-reliability aerosol target (LRAT) caused by cloud
248 contamination, solar noise contamination, especially in the daytime, and ground clutter
249 among mostly aerosol observations skews the distribution of the aerosol EC toward
250 larger values (Thomason and Vernier, 2013). Consequently, to eliminate the LRAT, a
251 statistical approach to identify LRAT, and extreme outliers is utilized based on the
252 interquartile range (IQR). IQR is a more conservative measure of the spread of
253 distribution than standard deviation (Iglewicz and Hoaglin, 1993). Note that this
254 technique is based on median statistics rather than the mean due to the skew distribution
255 of EC. In our implementation, we use daily data at each altitude (0.06 km) and latitude
256 (0.05°) bin from 2007-2020 to determine an EC frequency distribution for different
257 months. Besides, we used the lower quartile (Q1) and upper quartile (Q3) of the
258 underlying distribution to find IQR, defined as $Q3 - Q1$, a good measure of the spread in
259 the data relative to the median. Here, an extreme outlier is defined as $Q3 + (3.5 \times IQR)$,
260 and a more upper outlier ($Q3 + (1.5 \times IQR)$) is used for comparison (Iglewicz and Hoaglin,
261 1993). Meanwhile, the extreme outlier threshold is used to clear LRAT-affected
262 observations from the data set, which is better and more effective at identifying outliers
263 in the density distribution (Kovilakam et al., 2020).

264 **2.3 AI Data processing**

265 According to the method described in section 2.2, the aerosol EC (observed at 532
266 nm and 1064 nm for daytime and nighttime) with higher reliability over the TP is
267 obtained. The monthly mean Ångström exponent (hereafter “pseudo-Ångström
268 exponent(AE)”) between daytime and nighttime is derived to establish the 14-year
269 aerosol climatology (2007-2020) based on equation (1). The AE model for EC
270 wavelength dependence for 532 and 1064 nm is given by (Kovilakam et al., 2020):



$$EC_{-532[m,i,j]} = EC_{-1064[m,i,j]} \left(\frac{\lambda_{532}}{\lambda_{1064}} \right)^{AE[m,i,j]}, \quad (1)$$

where EC_{532} [m, i, j] and EC_{1064} [m, i, j] are extinction coefficient at 532, and 1064 nm, respectively; AE [m,i,j] is the pseudo-Ångström exponent (Rieger et al., 2015; 2019); and the indices [m, i, j] represent the month, latitude, and altitude respectively. $(\lambda_{532}/\lambda_{1064})$ represents the ratio of wavelengths at 532 and 1064 nm. The AE is gridded to 0.05° latitude and 0.06 km altitude resolution. Further, the vertical distribution of the new parameter AI is calculated according to equation (2). AI has been developed by (Nakajima et al., 2001; Liu et al., 2019):

$$AI_{[m,i,j]} = AOD_{[m,i,j]} \times AE_{[m,i,j]}, \quad (2)$$

where $AI_{[m,i,j]}$ and $AOD_{[m,i,j]}$ are aerosol index and aerosol optical depth, respectively; $AE_{[m,i,j]}$ is the pseudo-Ångström exponent; and [m, i, j] represent the month, latitude, and altitude respectively. Note that to match the AE , AOD is also transformed into the vertical distribution (not the column parameter). The monthly mean climatology of AI is computed in altitude and latitude for 532 and 1064nm between daytime and nighttime.

2.4 Aqua-MODIS data

Like CALIPSO, Aqua is part of the A-Train constellation of satellites. Therefore, MODIS (Moderate-resolution Imaging Spectroradiometer) onboard Aqua can achieve near-simultaneous observations of clouds and aerosols with CALIPSO-CALIOP (less than two minutes) (Winker et al., 2007; Hu et al., 2010). The Aqua satellite was successfully launched on May 4th, 2002. Aqua is the afternoon star, passing through the equator from south to north at around 13:30 local time. The observation data of 36 wavebands were obtained, with a maximum spatial resolution of 250 m and a scanning width of 2330 km. MODIS is a passive imaging spectroradiometer, there are a total of 490 detectors distributed in 36 spectral bands, with full spectral coverage ranging from 0.4 microns (visible light) to 14.4 microns (thermal infrared). In this study, Level 3 data (MYD08_M3) on a $1^\circ \times 1^\circ$ (longitude \times latitude) gridded box is utilized. As shown in Table 1, MODIS can provide 550 nm AOD and AE products. It is worth mentioning that we chose this data because MODIS data is widely used and has certain reliability



299 in aerosol research. The parameters of AE and AOD from MODIS are also used to
 300 calculate the AI, which is applied to evaluate the monthly mean climatology of AI from
 301 CALIOP over TP (see Table 1).

302 Table.1 Comparison between MODIS and CALIOP existing data products (√ represents the existing
 303 data products of the satellite, × represents data parameters that need further calculation in this
 304 study).

Detector/Satellite	Wavelength	Extinction Coefficient (EC)	Aerosol Optical Depth (AOD)	Angstrom Exponent (AE)	Aerosol Index (AI)
CALIOP/CALIPSO (active)	532&1064nm	√	√	×	×
MODIS/Aqua (passive)	550nm	×	√	√	×
				verification	verification

305

306 2.5 Ground-based LIDAR data

307 Besides, we use the ground-based LIDAR (Light Detection And Ranging) (38.967 °
 308 N, 83.65 ° E, 1099.3m) detection data from the hinterland of the Taklimakan Desert
 309 (TD) to verify the validity and accuracy of the low confidence aerosol removal method
 310 and the AI calculated by CALIOP detection data. Multi-band Raman polarization
 311 LIDAR (hereafter LIDAR) is mainly used for the detection of dust, aerosols, and clouds
 312 particles in the atmosphere, which detection belongs to “Belt and Road” Lidar Network
 313 from Lanzhou University, China (<http://ciwes.lzu.edu.cn/>), has an advantage with
 314 calibrate or validate Satellite observation (see Figure 2). The primary technical
 315 specifications of LIDAR are as given in Table 2. For the performance of this LIDAR
 316 and the data inversion of aerosol related optical parameters, the authors advise the
 317 readers to refer the research work of Zhang et al. (2022 and 2023).



318

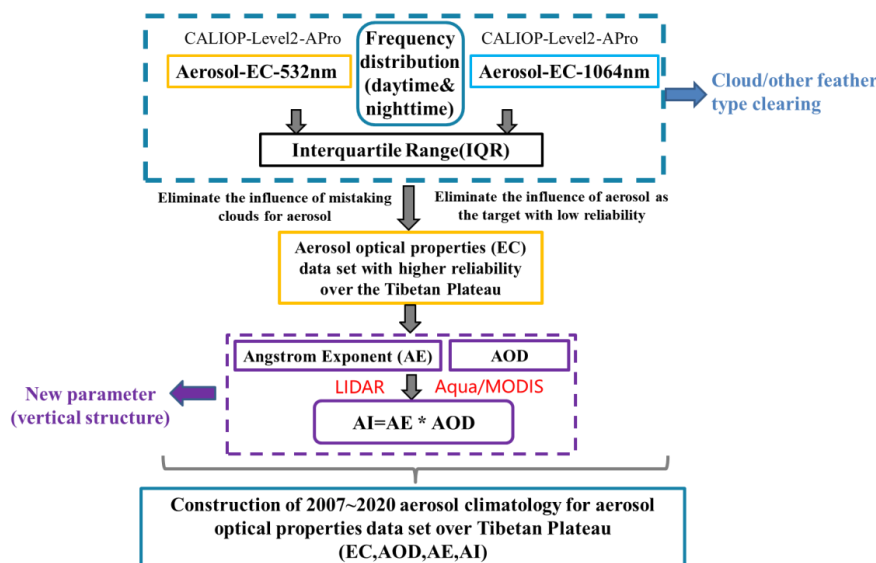
319 Figure 2. CALIPSO satellite orbit passes through the central area of the Taklimakan Desert
320 hinterland-left (the red triangle represents the observation coordinates of the ground-based LIDAR
321 - right (38.967° N, 83.65° E, 1099.3m), TD - Taklimakan Desert, TP - Qinghai Tibet Plateau)
322 (pictures from NASA'S Earth data (left) and photography(right)).

323 Table 2. Basic technical specifications of LIDAR from the hinterland of the Taklimakan Desert (TD).

Detection range	Spatial resolution	Laser wavelength	Laser energy	Pulse frequency
0~20km	7.5m	532nm/1064nm	100mJ	20Hz

324

325 In this study, based on the Level_2 aerosol profile data product (extinction
326 coefficient, EC) for daytime and nighttime detected by CALIOP from 2007 to 2020,
327 the low-reliability aerosol target (LRAT) is screened and eliminated. The aerosol
328 characteristic data set with higher reliability over the TP is constructed, and the data set
329 is verified and compared with MODIS and ground-based LIDAR to test its
330 effectiveness and accuracy. Thus, the vertical structure of aerosol characteristics
331 climatology with higher reliability over the TP can be obtained, providing adequate
332 observation facts and a basis for the TP. All steps were implemented and was processed
333 as follows in figure 3.



334

335 Figure 3. Flow chart of the aerosol characteristic data set construction and calculation process over
 336 TP.

337 3 Results and analysis

338 3.1 Low-Reliability Aerosol Target (LRAT) screened and eliminate

339 In this section, we screened and eliminate LRAT for tropospheric aerosol
 340 extinction coefficient (EC) from the available CALIOP profile products over the TP,
 341 based on the statistical method (see Section 2.2). Figures 4 and 5 show the monthly
 342 frequency distribution of EC at 532 nm and 1064 nm in the daytime during 2007-2020
 343 from January to December was detected by the CALIPSO-CALIOP troposphere within
 344 12 km. While Figures 6 and 7 are for nighttime. Generally, Figures 4-7 demonstrate the
 345 non-normal distribution for EC. We found that the upper outlier appeared to remove
 346 many enhanced aerosol measurements, when more sand and dust events occurred in the
 347 surrounding areas and rose to the TP in spring and summer. In contrast, the extreme
 348 outlier was effectively identified in the frequency distribution. Therefore, the extreme
 349 outlier threshold used to clear LRAT observations from the CALIOP data set is
 350 necessary.

351 After the LRAT of screened and eliminate, we can directly compare these

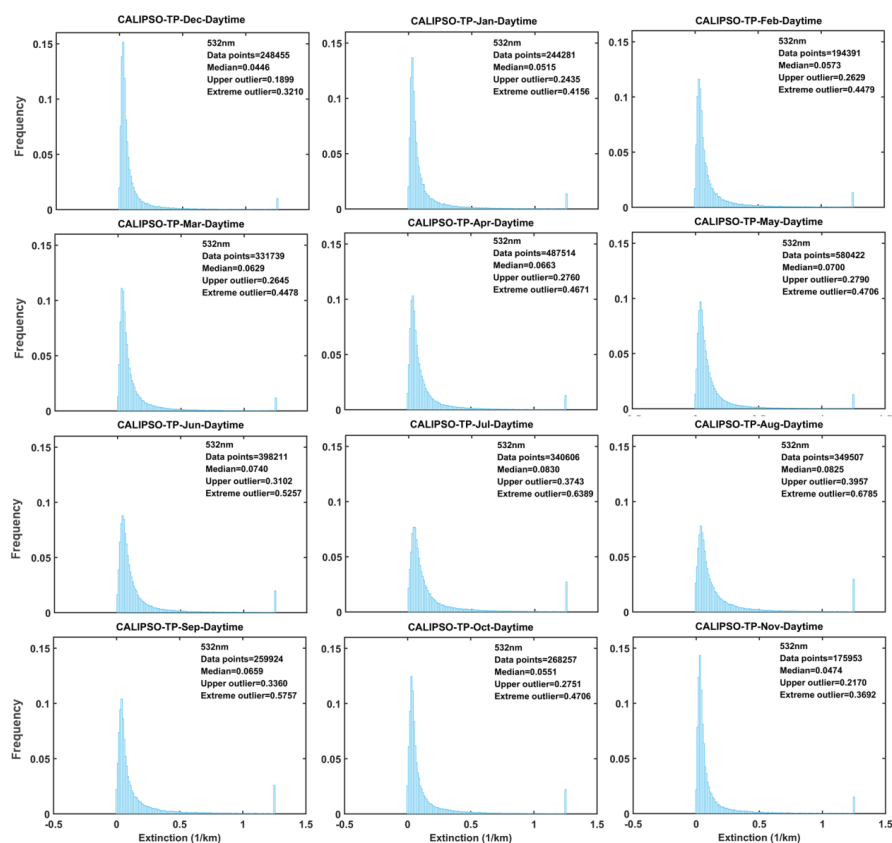


352 measurements of the monthly climatology of data points and extreme outliers (2007 –
353 2020). We found that during the daytime for 532 nm and 1064 nm, the aerosol EC over
354 the TP is mainly concentrated between 0 and 0.2. The extreme outliers in July and
355 August are more significant than those in other months, which may be related to the
356 rising motion of the TP as a heat source in summer to trigger convection, resulting in
357 more ice clouds in the upper air, thus increasing the probability of misclassification the
358 cirrus anvil as an aerosol (Carrió et al., 2007; Kojima et al., 2004; Seifert et al., 2007).
359 Also, the aerosol data points (samples) is the largest in May and the smallest in
360 November over TP; Obviously, spring and summer are more than autumn and winter;
361 This is related to the frequent sand and dust activities in spring and summer around the
362 TP (such as Taklimakan Desert) and anthropogenic pollution (as mentioned earlier).

363 Similarly, during the nighttime for 532nm and 1064nm, the aerosol EC over the
364 TP is mainly concentrated between 0 and 0.1, and the extreme outliers in July and
365 August are still greater and more significant than those in other months. Still, it is
366 smaller than the daytime data set. The primary consideration is that the daytime solar
367 noise is considerable and the signal-to-noise ratio of LIDAR observation is low, which
368 further increases the probability that the aerosol EC presents skewed distribution; It can
369 be seen that the removal of LRAT from daytime data is more conducive to improving
370 the accuracy of data. Meanwhile, the aerosol data points are the largest in April and the
371 smallest in December over the TP. It can be seen that in April (spring), more aerosol
372 samples were lifted and transported to the TP. Numerous observations have shown
373 elevated dust plumes lofted into the free troposphere during spring, and air parcels
374 between 4 km and 7 km mainly originate from TD (Huang et al.,2008; Sasano,1996;
375 Liu et al.,2008; Zhou et al.,2002; Matsuki et al., 2003). It is the same as the daytime
376 with spring and summer being more than autumn and winter while there is one order of
377 magnitude larger than the data point in the day. It is not difficult to see that the main
378 reason is that the CALIOP is less sensitive during daytime than nighttime due to signal-
379 noise-ratio reduction by solar background illumination, which leads to weakly
380 scattering layers can be detected during nighttime while missed during daytime (Huang
381 et al., 2013; Liu et al.,2009).



382



383

384 Figure 4. Monthly frequency distribution of aerosol extinction coefficient at 532nm over Tibet
385 Plateau (TP) daytime during 2007~2020 from January to December (Panels 1st stands for Winter for
386 Dec ~ Feb.; Panels 2nd stands for Spring for Mar ~ May; Panels 3rd stands for Summer for Jun ~
387 Aug; Panels 4th stands for Autumn for Sep ~ Nov). Frequency distribution is the number of events
388 normalized to the maximum value. Upper outlier and extreme outlier and median also have been
389 shown.

390

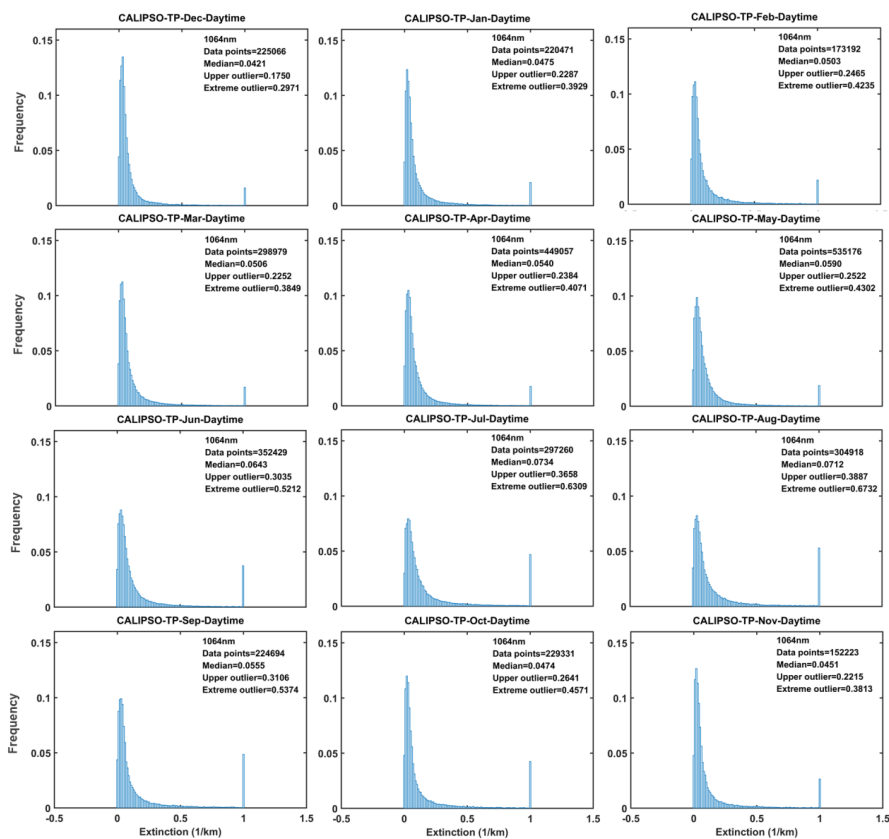
391

392

393

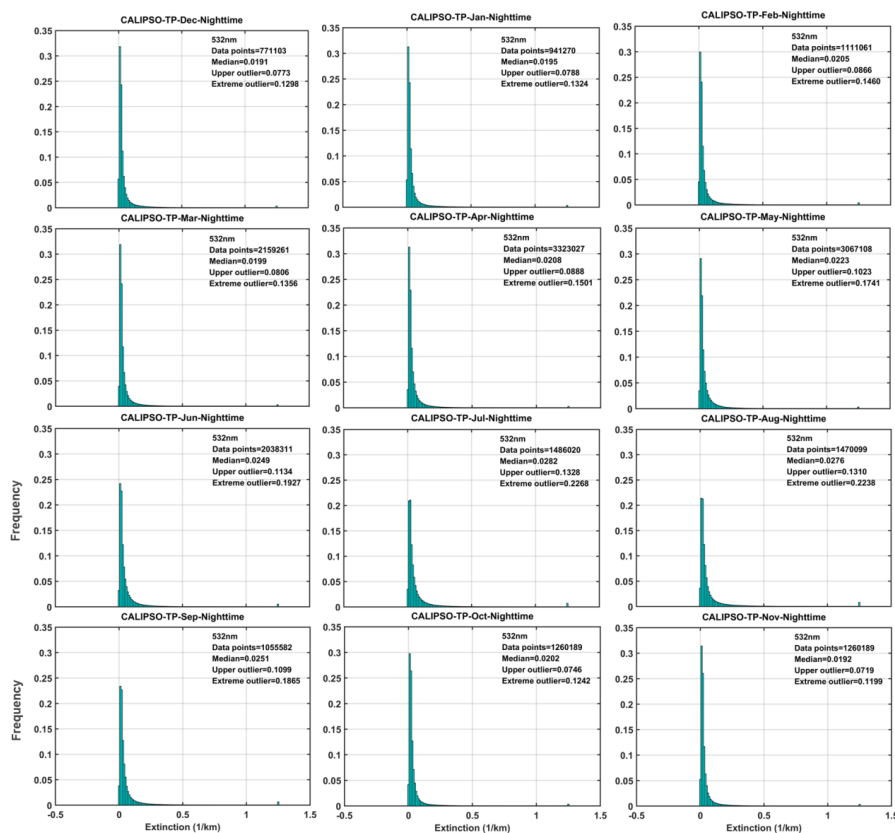
394

395



396
397 Figure 5. The same as in Figure 4 except for 1064nm.

398
399
400
401
402
403
404
405
406
407
408
409



410

411 Figure 6. Frequency distribution of aerosol extinction coefficient at 532nm over Tibet Plateau (TP)
412 nighttime during 2007-2020 from January to December (Panels 1st stands for Winter for December-
413 February; Panels 2nd stands for Spring for March-May; Panels 3rd stands for Summer for June-
414 August; Panels 4th stands for Autumn for September-November). Frequency distribution is shown
415 as the number of events normalized to the maximum value. Upper outlier and extreme outlier, and
416 median also have been shown.

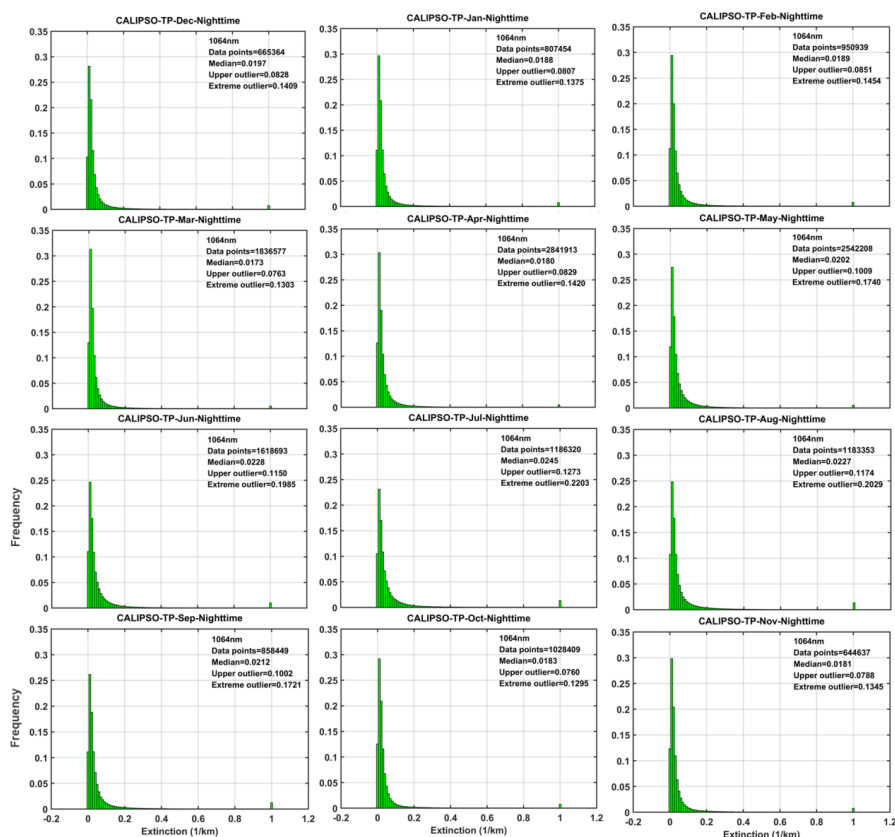
417

418

419

420

421



422
423 Figure 7. The same as in Figure 6 except for 1064nm.
424

425 3.2 Constructing vertical aerosol index (AI) for daytime and nighttime

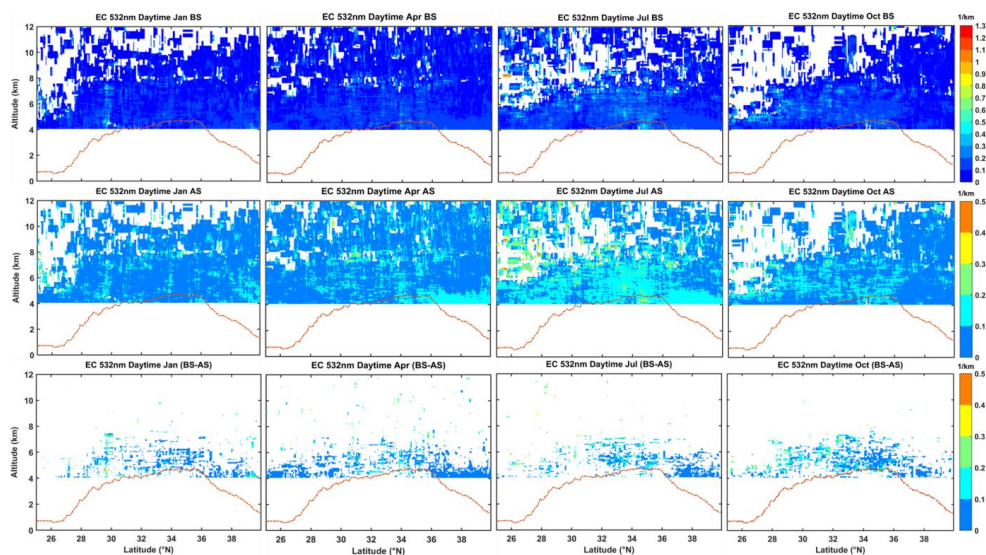
426 Figures 8 and 9 show daytime altitude-latitude plots of the monthly climatology
427 of the aerosol EC with 532 nm and 1064 nm before and after screen, respectively. The
428 monthly mean climatology of the pseudo-Ångström exponent (AE) and Aerosol Index
429 (AI) vertical structure is then computed (as shown in figure 10). We choose January,
430 April, July and October to represent winter, spring, summer and autumn (same as
431 below). Figures 8 and 9 show that extreme outliers in the troposphere over the TP have
432 been eliminated, especially in the lower layer, where more obvious LRAT have been
433 identified and eliminated. In the upper layer (more than 7 km), especially in April and
434 July (i.e., spring and summer), weak cirrus signs may exist in the original aerosol
435 signals and be eliminated. Compared with other seasons, the aerosol on the TP is widely
436 and uniformly distributed in the troposphere in April, indicating that in general, more



437 aerosol loads are lifted over the TP in April. In figure 10, we compute values between
438 0 and -1 for much of the troposphere and occasionally are between 0 and 2 in the middle
439 troposphere (less than 8 km), which has similar results or pattern in Kovilakam's study
440 (Kovilakam et al., 2020). Note that the derived value for pseudo AE is without the
441 physical meaning, and it is simply a means to combine AOD to obtain AI of vertical
442 structure. Using this climatology of pseudo-AE values, we can effectively convert any
443 month of AI data to 532 nm and 1064 nm because the fixed AE is not necessarily
444 applicable to retrieving aerosol extinction in all months. Relevant research points out
445 that the accuracy has been improved, that is, using the corresponding AE index of each
446 month to correct the satellite data (Kovilakam et al., 2020).

447 Figure 10 also demonstrates the distribution characteristics of AI values at 532nm
448 and 1064nm in different seasons over the TP in the daytime. In all seasons, AI is mainly
449 distributed between -0.04 and 0.04. Still, the proportion between 0 and -0.02 is the
450 largest, indicating that the proportion of non-absorbability of tropospheric aerosols over
451 the TP is greater than that of absorbability of particles (AI, positively suggests the
452 existence of absorbent aerosols (dust, black carbon, etc.); A small or negative AI
453 suggests the presence of non-absorbable aerosols or clouds) (Hu et al.,2020; Guan et
454 al., 2010; Hammer et al., 2018). In cloud-free conditions, the highest and thickest
455 absorbing aerosols with the most prominent AI values, AI varies with aerosol layer
456 height, optical depth and single scattering albedo (Torres et al., 1998; 2007; Hsu et
457 al.,2004). In the four seasons, the distribution of aerosols in the north is broader than that
458 in the south; In spring, the rise height of aerosol is higher and the vertical distribution
459 range is more comprehensive; The elevation in summer is lower than that in the other
460 three seasons, but the aerosol species are more abundant, because there are many ranges
461 of AE values; However, the absorption aerosol below 7km in summer is less than that
462 in other three seasons.

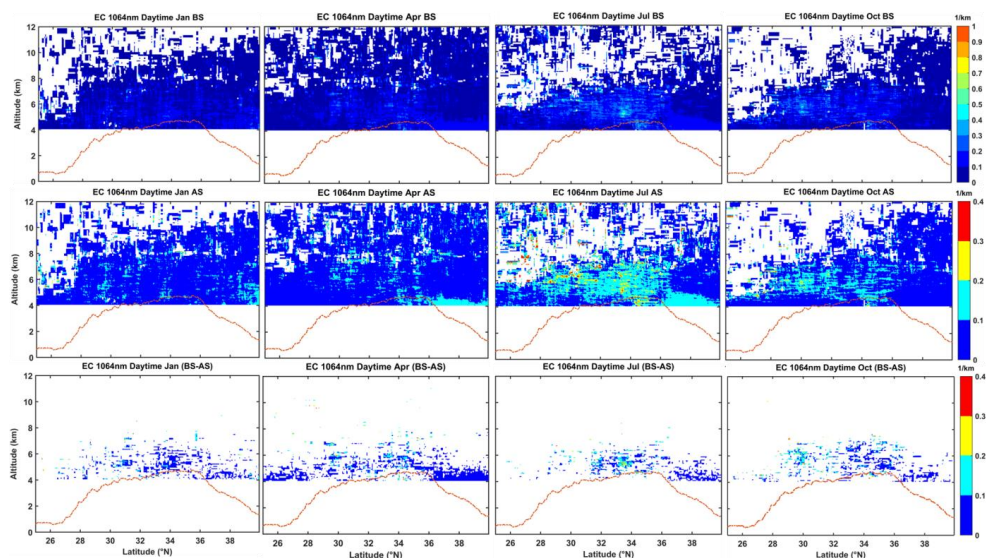
463



464

465 Figure 8. The monthly average comparison and difference of 532nm aerosol extinction coefficient
466 before and after low-reliability aerosol target (LRAT) removal over Tibet Plateau (TP) daytime
467 during 2007-2020. The reddish-brown dotted line denotes the surface. (BS: Before Screened, first line;
468 AS: After Screened, second line; (BS-AS) means Before Screened minus After Screened,
469 representing spatial lattice with screening and elimination, third line)

470

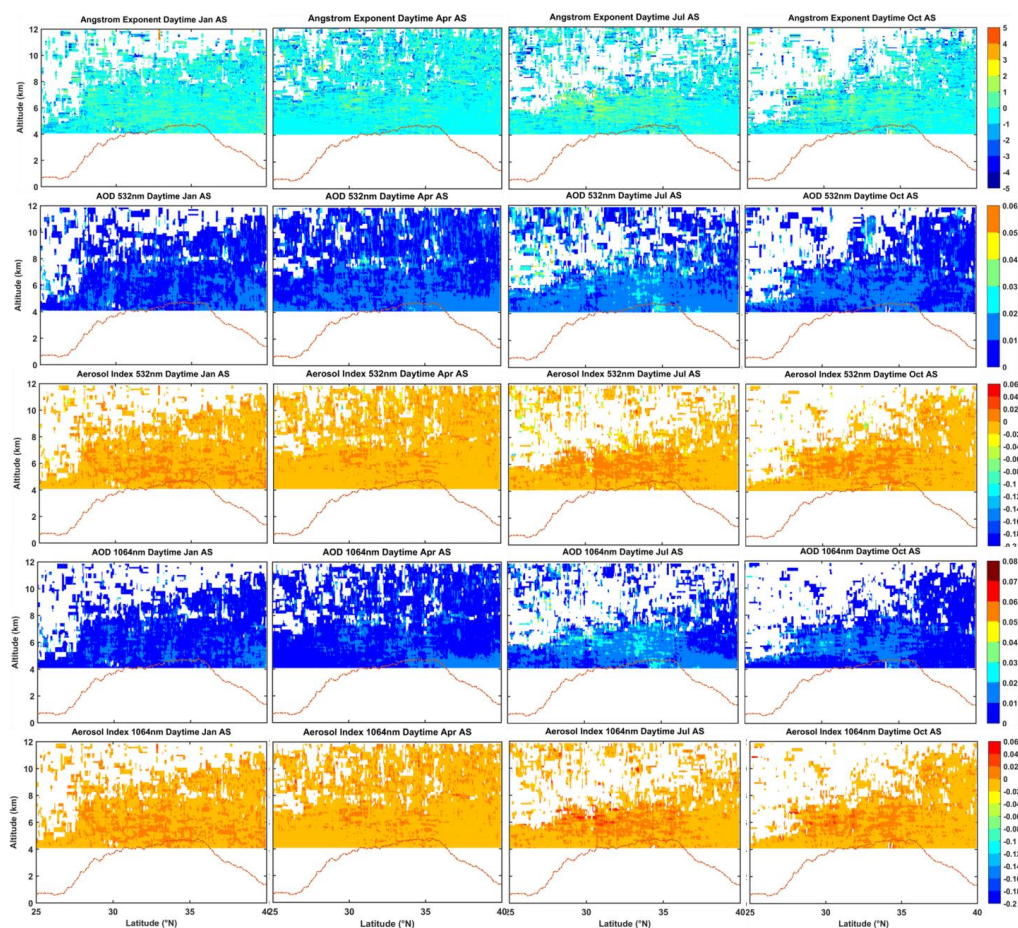


471

472

Figure 9. The same as in figure 8, but for 1064 nm.

473



474

475 Figure 10. The monthly average construction of Angstrom Exponent (AE) and Aerosol Index (AI)
476 of vertical structure for 532nm & 1064nm over Tibet Plateau (TP) daytime during 2007-2020.

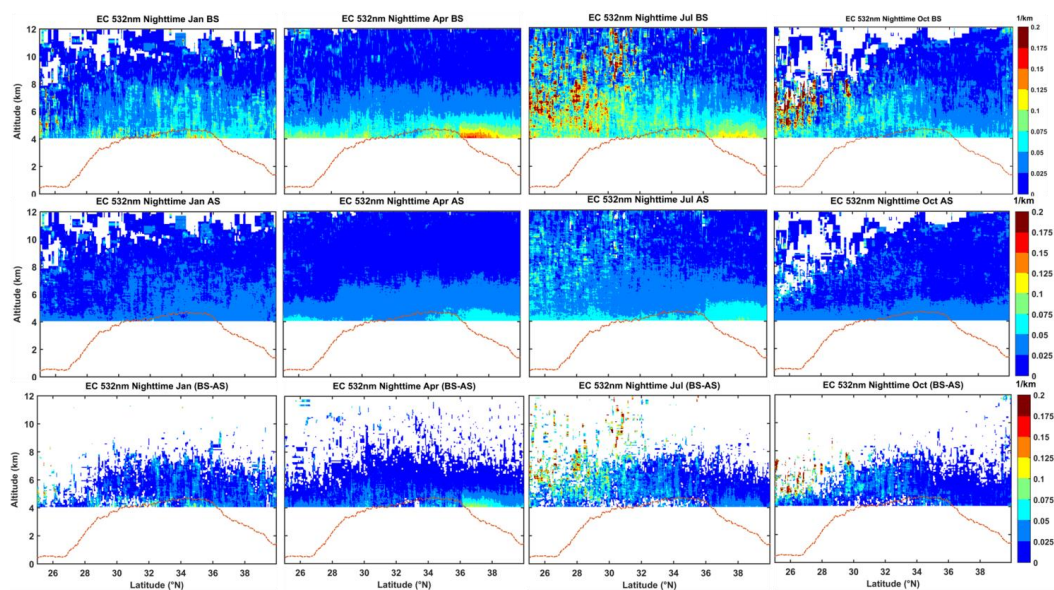
477

478 Similarly, figure 11 includes the nighttime difference plots between the before-
479 screened CALIOP 532nm EC and after-screened for different months during 2007-2020.
480 The difference before and after screening is immense, especially at the height of more
481 than 5 km in the southern region of the TP in July and October. We can see extreme
482 outliers in the troposphere over the TP that have been recognized and eliminated. The
483 EC detected at CALIOP 1064 nm shows a similar distribution characteristic as 532 nm,
484 and also includes the different attributes before and after the screened and removal of
485 LRAT (see as figure 12). In all seasons, AI is mainly distributed between -0.02 and 0.02.
486 Still, the proportion between 0 and -0.02 is the largest in April and July (especially in



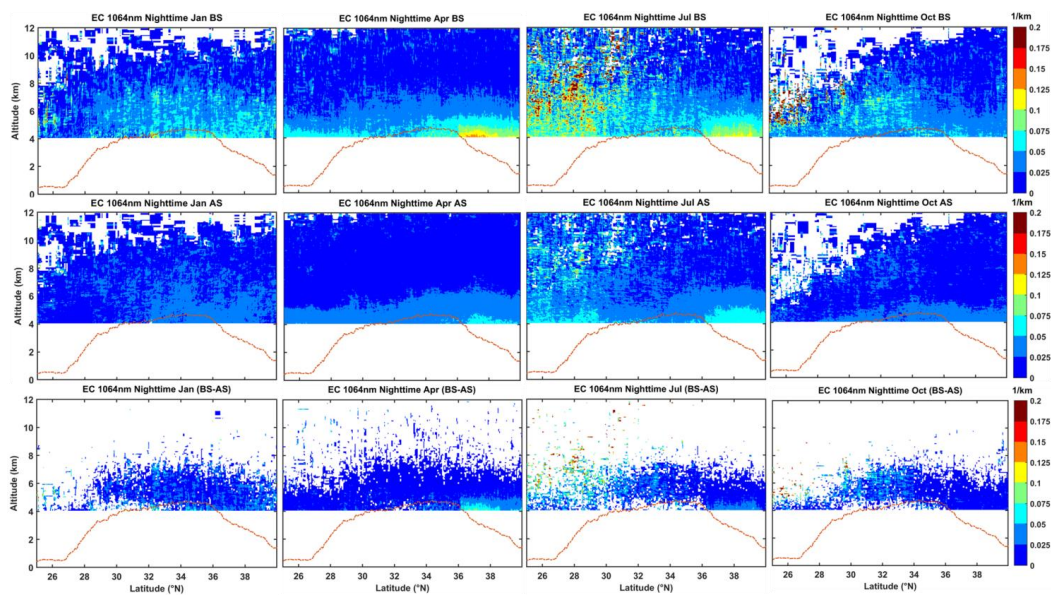
487 April, the non-absorbable aerosols dominate the 4-8 km high layer of the TP), indicating
488 the presence of non-absorbable aerosols. Meanwhile, AI above 8 km is mainly
489 concentrated at 0~0.02, indicating that the absorption aerosol is dominant. It is worth
490 noting that there is a large amount of absorbent aerosol over the TP in January (winter),
491 related to anthropogenic emissions of pollutants in winter and fossil fuel combustion
492 (such as black carbon and smoke). We note the pattern of AI is more or less consistent
493 with objective facts and phenomena.

494 Interestingly, compared with the daytime, the aerosol detected by CALIOP at night
495 can rise to a higher height and has a broader distribution range. It can be seen that
496 because the signal-to-noise ratio at night is higher than that in the daytime, CALIOP
497 can detect smaller particles, which is also why the quality and effectiveness of CALIOP
498 night detection data is better than that in the day. After a series of correction algorithms
499 and calculating relevant parameters, we have constructed the tropospheric AI
500 climatology dataset over the TP for 2007-2020.



501

502 Figure 11. The same as in figure 8, but for nighttime.



503

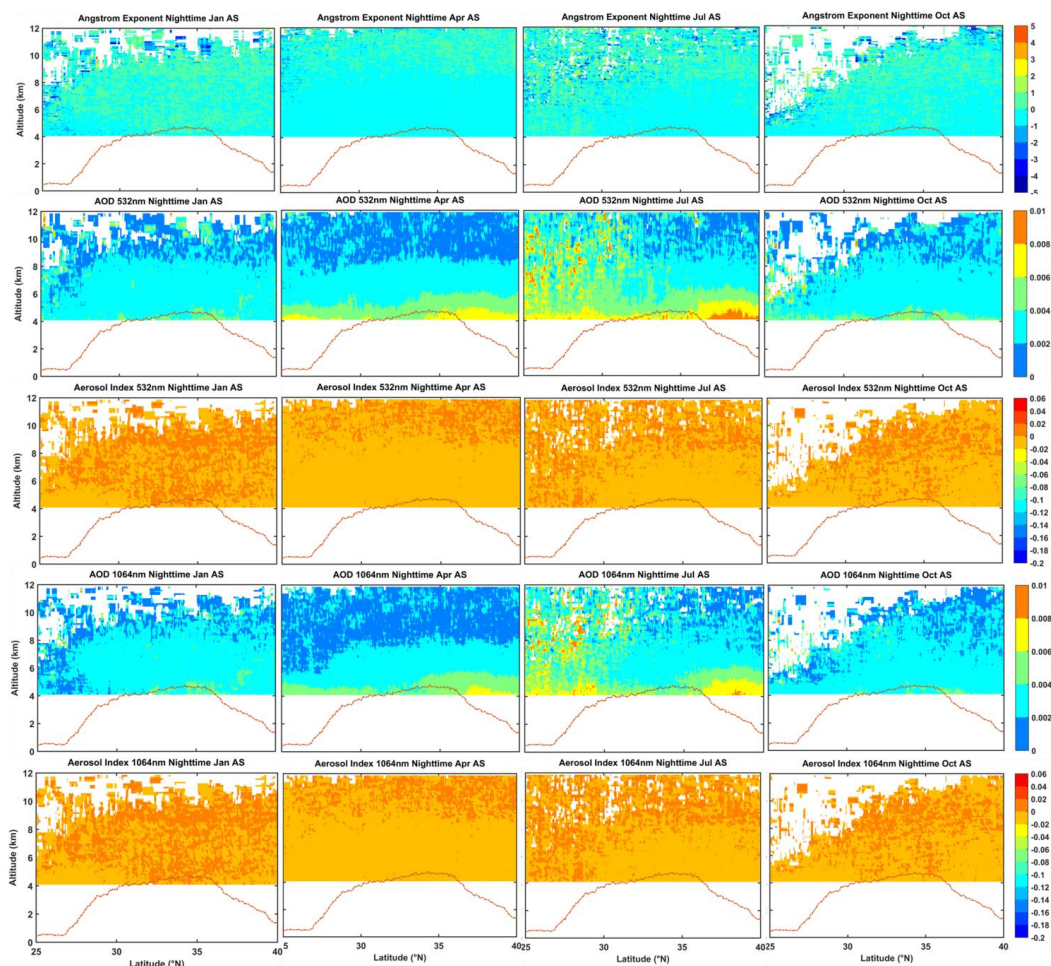
504 Figure 12. The same as in figure 11, but for 1064nm.

505

506

507

508



509

510 Figure 13. The same as in figure 10, but for nighttime.

511 3.3 Validation of the aerosol index (AI) dataset

512 3.3.1 Comparisons with satellite Aqua-MODIS AI products

513 The multiyear monthly average spatial distributions of the AE and AOD from
514 MODIS have been shown in figure 14, and AI was also calculated (Figure 14). The
515 distribution of AE values over the TP in all seasons shows a decreasing trend from
516 southeast to northwest, indicating that the particles in the upper air of the southeast
517 region are dominated by small particles. In contrast, the particles in the upper air of the
518 northwest region are dominated by large particles, especially in April of spring, which
519 is related to the uplift and transmission of dust aerosol from the Taklimakan Desert to



520 the northern part the TP in spring. Additionally, we can see that the AE value of
521 Taklimakan Desert in the north of the TP in April and July in spring and summer is
522 smaller (as the source of the sand area, mainly dust aerosol), which is smaller than in
523 January and October in autumn and winter; AOD and AE showed opposite seasonal
524 variation distribution patterns. According to the spatial distribution pattern of AI
525 calculated from MODIS detection results (AE and AOD), it can be seen that the AI
526 value over the TP is mainly between 0 and 0.4. It shows that the primary existence is
527 an absorbent aerosol.

528 Figure 14 also compares the normalized frequency distribution of AI over the TP
529 exhibiting a significant difference in all seasons from MODIS and CALIOP between
530 BS and AS. It is evident that, in general, compared with the actual data results without
531 any processing, after removing the low-reliability aerosol target, the average AI value
532 of CALIOP is closer to the result of MODIS, and the normalized frequency distribution
533 pattern is closer to the same. Interestingly, the AI mean value and normalized frequency
534 distribution pattern of CALIOP in April (spring) after removing the LRAT are more
535 agreement and matched with the results of MODIS; In addition, the AI mean value and
536 normalized frequency distribution pattern of CALIOP in July (summer), and October
537 (autumn) is more consistent with the MODIS results, and both have apparent
538 improvement; The difference between the AI average value of CALIOP in January
539 (winter) and the result of MODIS is relatively more extensive, but the normalized
540 frequency distribution pattern is more consistent. This may be related to the type and
541 chemical composition of aerosol particles that rise over the TP in different seasons and
542 the atmospheric climate conditions unique to the topography of the TP. In brief, the
543 accuracy of aerosol parameters AI calculated after obtaining aerosol EC with higher
544 reliability has been dramatically improved (more or less), so even though not
545 completely accurate, this strategy is expected to reduce the inaccuracy of the computed
546 AI at least.

547 Meanwhile, it is proved that using extreme outliers as a limit to get more reliable
548 aerosol detection information is effective and reliable. It is important to note that the
549 550 nm wavelength range of MODIS belongs to the visible light range, and the data



550 products provided at the satellite transit time are the daytime detection results.
551 Therefore, here we compare and verify the daytime detection results of CALIOP (532
552 nm) with MODIS results, which are consistent in time, close in detection wavelength,
553 comparable, and representative. In addition, the quality of CALIOP daytime detection
554 data is inferior to that at night, and the reliability and accuracy of the optimized data
555 are more effectively verified by comparison with the results of MODIS. Passive
556 techniques (i.e., MODIS) have the advantage of providing a 2-D distribution of AI over
557 a wide swath, during active strategies (i.e., CALIOP) with AI vertical structure. They
558 are complementary and have their advantages.

559

560

561

562

563

564

565

566

567

568

569

570

571

572

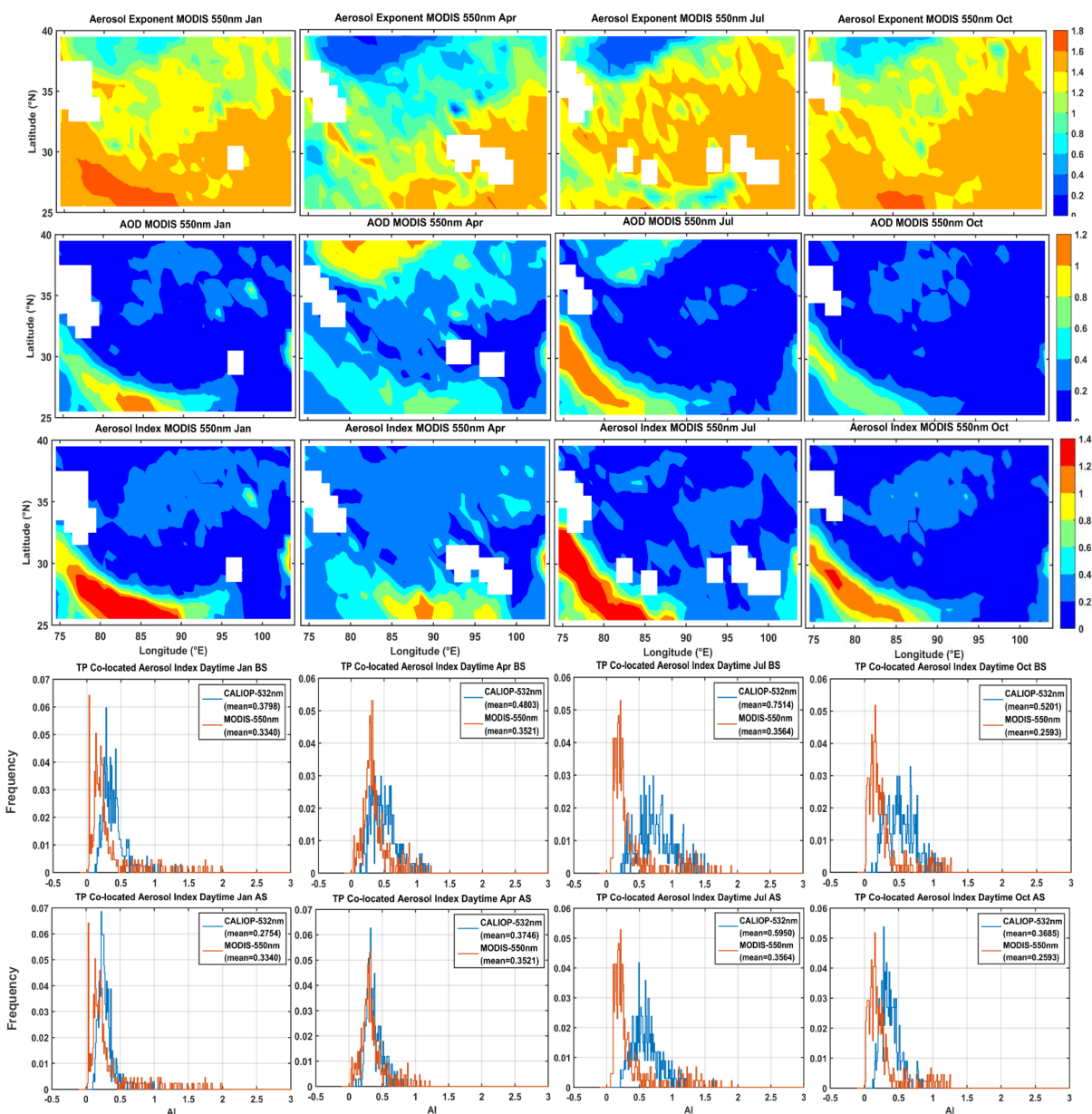
573

574

575

576

577



578 Figure 14. Frequency test of AI calculated by MODIS-based aerosol AE and AOD over the Qinghai
 579 Tibet Plateau and AI calculated by CALIPSO-based aerosol AE and AOD with high reliability for
 580 daytime (BS: Before Screened, the fourth line; AS: After Screened, the fifth line).

581 3.3.2 Performance evaluation based on in-situ Lidar observations

582 To further verify the performance of the AI product derived from CALIOP over

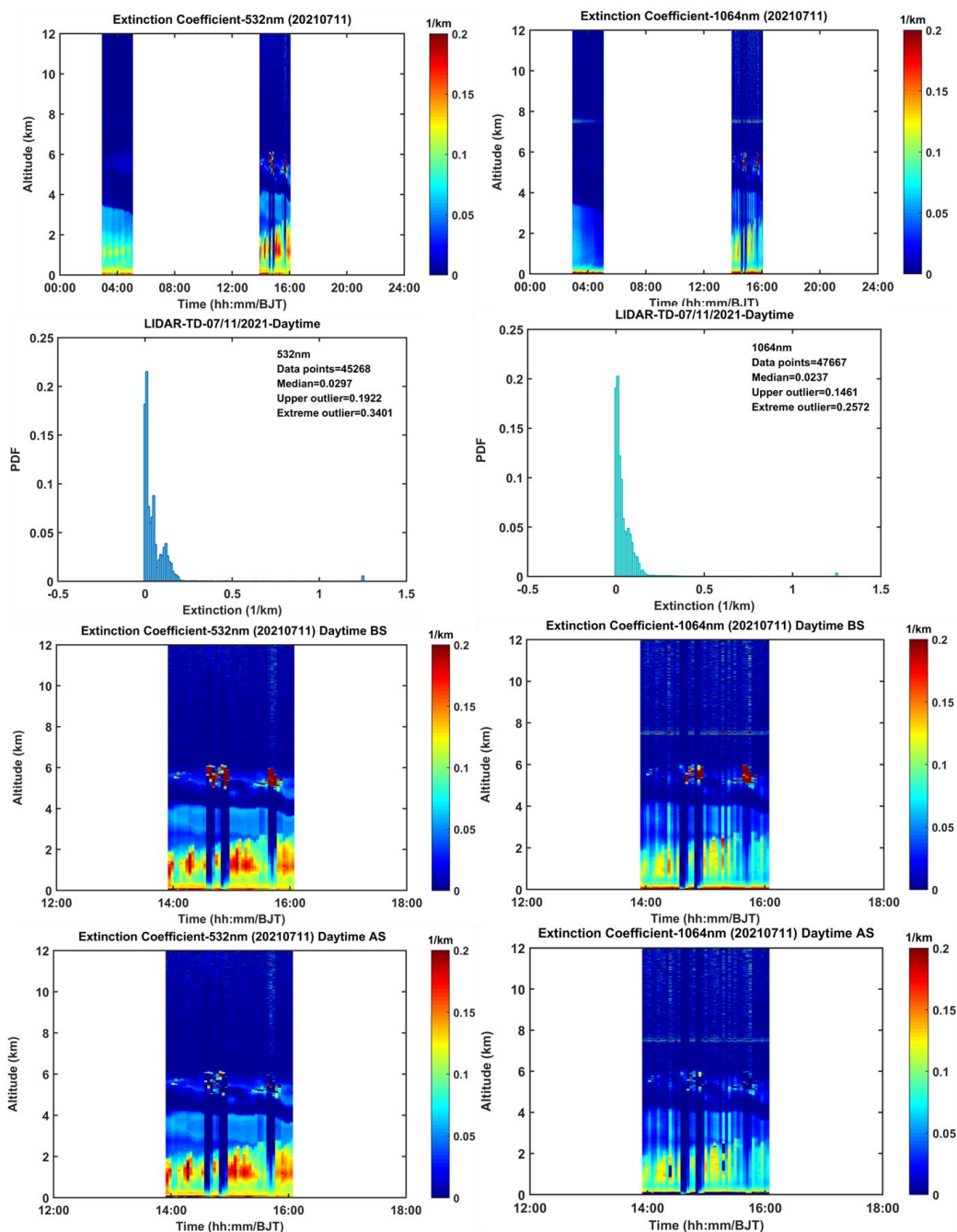


583 the TP, we chose to use the ground-based LIDAR observation results in the center of
584 the Taklimakan Desert in the north of the TP to evaluate the effectiveness and accuracy
585 of the AI vertical structure of CALIOP.

586 To match the transit time of ground-based LIDAR observation and satellite
587 CALIOP observation, we extracted the EC (532 nm and 1064 nm) of ground-based
588 LIDAR during the daytime and nighttime to match the CALIOP adjacent observation
589 period, as shown in Figure 15 (observation case in TD on July 11, 2021, daytime: 03:00-
590 05:00, night: 14:00-16:00, China Beijing time, UTC+8). Considering the daytime
591 detection results of CALIOP for comparison and verification with MODIS in the above,
592 to further strengthen the inspection of CALIOP optimization results, we still choose the
593 daytime results of ground-based LIDAR detection for comparison and verification.
594 From Figure 15, it can also be seen that there are clouds or other LRAT in the daytime
595 high altitude in the ground-based LIDAR detection signal. This will be more beneficial
596 for us to check the validity and reliability of the results of the elimination of LRAT and
597 the calculated AI value.

598 Similarly, for ground-based LIDAR detection, we first reverse EC and use the IQR
599 method (see sec.2.2) to obtain extreme outliers and identify and eliminate the LRAT
600 (Figure 15). We can see that the LRAT (such as clouds and surface clutter etc.) are
601 effectively eliminated after the data optimization of 532nm and 1064nm detection
602 results EC. It is once again proved that it is effective and reliable to use extreme outliers
603 as a limit to obtain more reliable aerosol detection information.

604
605
606
607



608 Figure 15. Removal of low-reliability aerosol target signals detected by ground-based LIDAR in the
609 hinterland of Taklimakan Desert.

610

611 It is needed to be pointed out that the case of ground-based LIDAR detection on

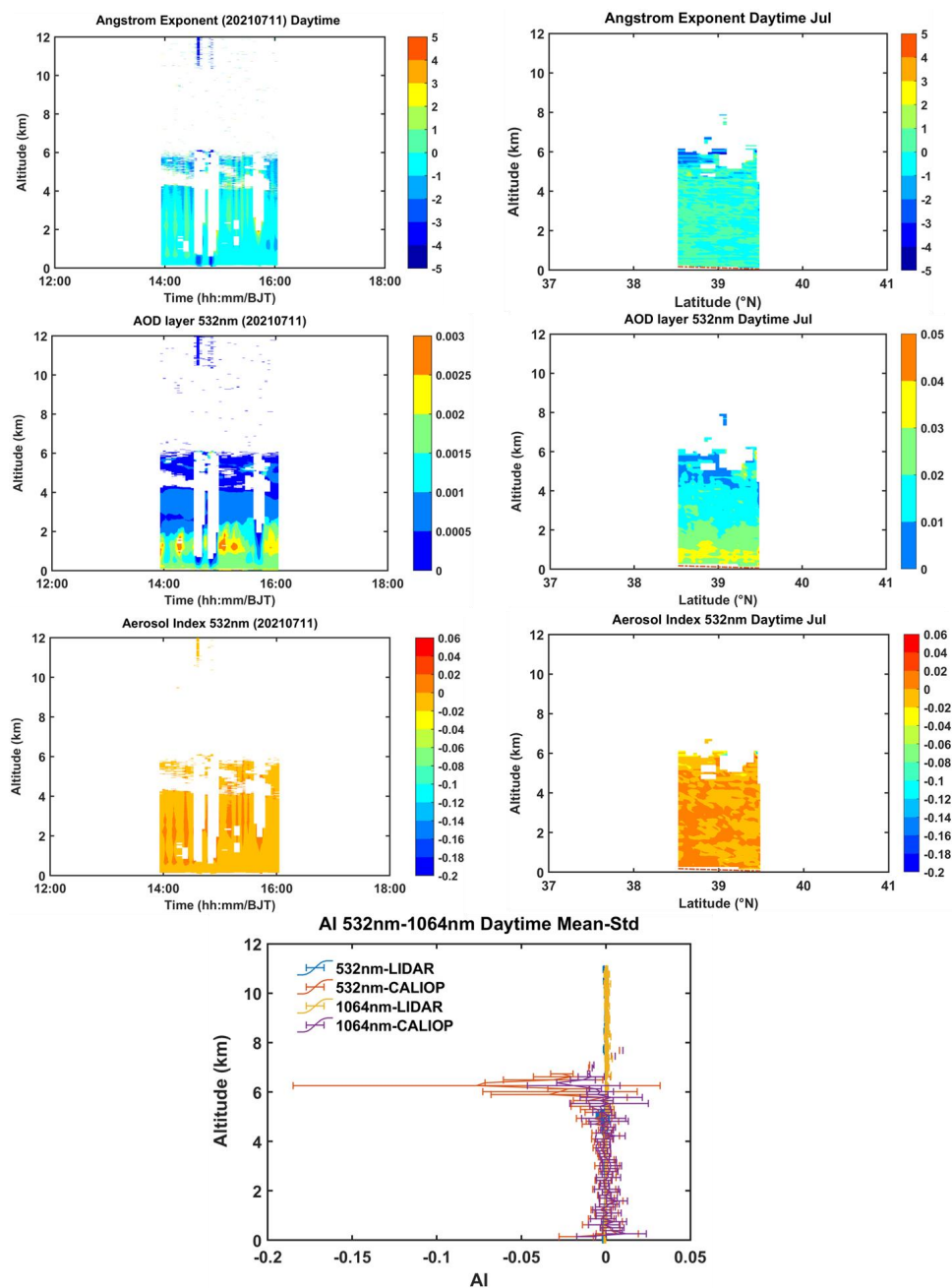


612 July 11, 2021 is quite typical, but there is a significant deviation in satellite transit, and
613 this process cannot be well captured. To maximize and better match this process, we
614 take the ground-based LIDAR observation in the hinterland of the Taklimakan Desert
615 as the center (38.967° N, 83.65° E, 1099.3m), select $38.5\sim 39.5^{\circ}$ N and $83\sim 84^{\circ}$ E
616 range, extract the ECs observed by CALIOP transit in this range during the daytime
617 from 2007 to July 2020, and eliminate the LRAT. After averaging the optimized data,
618 further, calculate the AE value (as shown in Figure 16). Figure 16 depicts the detection
619 results of ground-based LIDAR and CALIOP optimal crossing point and the
620 comparison of calculated AI values. The AE values detected by ground-based LIDAR
621 and CALIOP are mainly distributed between - 1 and 1, and the proportion between - 1
622 and 0 is the largest. The aerosol can be raised to the height of 6 km, and the higher
623 concentration of aerosol is mainly concentrated below 2 km from the AOD vertical
624 layer, showing a decreasing trend with the increase of height; AI values are primarily
625 distributed between -0.02 and 0.02, and the average value and standard deviation trend
626 of AI change with height are also basically consistent. Generally, all those facts
627 demonstrate the agreement of the AI dataset with the CALIOP and ground-based
628 LIDAR. Besides, all the evidence shows that after removing the LRAT, the optimized
629 data can obtain aerosol characteristics with higher reliability.

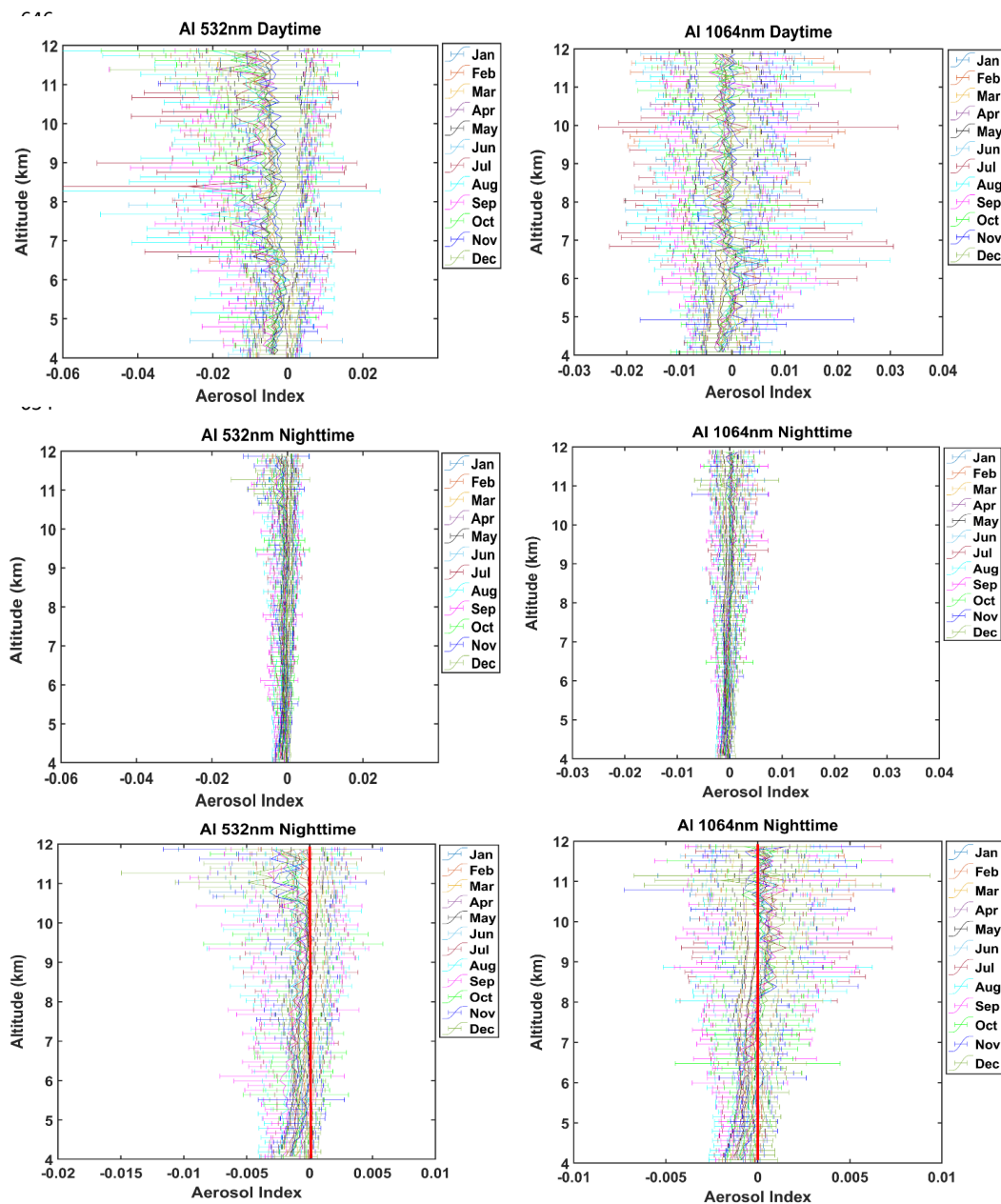
630 Based on the monthly climatology AI product, we explored average vertical
631 structure change characteristics of AI over TP during 2007-2020 (as shown in figure
632 17). AI values in the daytime and at night over the Qinghai-Tibet Plateau mainly
633 fluctuate around 0, and the standard deviation increases with the increase of altitude.
634 The trend of AI changes with altitude is relatively consistent, and the standard deviation
635 below 6 km is slight, indicating that the dispersion of aerosol particles is small.
636 However, the fluctuation in the daytime is greater than that at night (the data quality at
637 night is better than that in the daytime). In general, the detection results of 532 nm and
638 1064 nm can achieve complementary observation. From the AI results at night, it can
639 be seen that the AI value of 532 nm over the whole troposphere over the TP is less than
640 0 in all months, indicating the existence of non-absorbable aerosols or clouds. We have
641 eliminated the interference of clouds, so there may only be non-absorbable aerosols. In



642 addition, when we look at 1064nm and the height above 8km, AI is positive, indicating
 643 the existence of absorbent aerosols (dust and black carbon).



644 Figure 16. Comparative verification of AI of CALIPSO and ground-based LIDAR remote sensing
 645 in Taklimakan Desert.



671 Figure 17. Monthly average vertical structure change characteristics of AI (mean & standard
672 deviation) over TP during 2007-2020.

673

674

675



676 **4 Data availability**

677 Data described in this work are available at
678 <https://data.tpdc.ac.cn/en/disallow/03fa38bc-25bd-46c5-b8ce-11b457f7d7fd>
679 DOI:10.11888/Atmos.tpdc.300614. (Honglin Pan et al., 2023)

680

681 **5 Summary and outlook**

682 This present study is the first to report long-term, advanced-performance, high-
683 resolution, continuous and high-quality, monthly climatology aerosol AI vertical
684 structure from the CALIOP observation over TP which may be used to better
685 understand aerosol radiation forcing under the background of accelerated climate
686 change. Using the relationship developed when EC measurements are available, we
687 screened the entire EC record. We assembled a climatology of high-altitude aerosol
688 characteristics for daytime and nighttime from 2007 to 2020. In addition to providing a
689 monthly climatology AI data set for MODIS and ground-based LIDAR validation, our
690 data set also reveals the patterns and numbers of high-altitude vertical structure
691 characteristics of the aerosol troposphere over the TP.

692 To produce an accurate and higher reliability of AI values, we applied several
693 correction procedures and rigorously checked for data quality constraints during the
694 long observation period spanning almost 14 years (2007-2020). Nevertheless, some
695 uncertainties remain mainly due to technical constraints, as well as limited
696 documentation of the measurements. Even though not completely accurate, this strategy
697 is expected to at least reduce the inaccuracy of the computed characteristic value of
698 aerosol optical parameters. Following this initial work, we obtained vertical AI value
699 with higher reliability. This provides information about the vertical structures of aerosol
700 that could be used in climate models. The collection of more reliable and robust research
701 data sets of aerosol characteristics in these extreme environments is the key basis for
702 promoting comprehensive research on the energy balance of ground-atmosphere
703 radiation over the Tibetan Plateau and even the global region. We expect that this data
704 set will help some current and future research to simulate the climate change of the
705 monthly climatology. It will also help to update future data sets and study the interaction



706 of aerosol-cloud-precipitation, thus providing sufficient observation facts and basis.

707 **Author contributions.** HP led the reprocessing of the CALIOP, LIDAR, MODIS
708 measurements, data analysis and the preparation of the figures, with JH and JL both
709 contributing to design of the paper and progression of figures and text of the article. ZH
710 and TZ made the original LIDAR measurements. ZH provided the dataset and advice
711 on the re-processing of the LIDAR and CALIOP. KRK contributed to either
712 advising/co-ordinating the data recovery. All co-authors performed writing sections of
713 the paper, and/or reviewing drafts of the paper.

714

715 **Competing interests.** The authors declare that they have no conflict of interest.

716

717 **Acknowledgements.**

718 We are grateful to the CALIPSO (<https://eosweb.larc.nasa.gov/>), MODIS
719 (<https://ladsweb.modaps.eosdis.nasa.gov/>) instrument scientific teams at NASA for the
720 provision of satellite data, and “Belt and Road” Lidar Network from Lanzhou University,
721 China (<http://ciwes.lzu.edu.cn/>), which are available online and formed the central
722 database in the present work.

723

724 **Financial support.**

725 This work was financially Sponsored by the Natural Science Foundation of Xinjiang
726 Uygur Autonomous Region (Grant No. 2022D01B74), the Second Tibetan Plateau
727 Scientific Expedition and Research Program (STEP)(Grant No. 2019QZKK0602),
728 Scientific and Technological Innovation Team (Tianshan Innovation Team) project
729 (Grant No. 2022TSYCTD0007), National Natural Science Foundation of China (Grant
730 No. 42005074), Scientific Research and Operation Cost Project of Urumqi Institute of
731 Desert Meteorological, China Meteorological Administration (Grant No.
732 IDM2020003).

733

734 **References**

735 Bucci, S., Cagnazzo, C., Cairo, F., Liberto, L.D., Fierli, F.: Aerosol variability and



- 736 atmospheric transport in the Himalayan region from CALIOP 2007–2010
737 observations, *Atmospheric Chemistry and Physics*, 14(9): 4369-4381, 2014.
- 738 Boos, W., Kuang, Z.: Dominant control of the South Asian monsoon by orographic
739 insulation versus plateau heating, *Nature*, 436, 218-222, 2010.
- 740 Buchard, V., Da Silva, A. M., Colarco, P. R., Darmenov, A., Randles, C. A., Govindaraju,
741 R., Torres, O., Campbell, J., Spurr, R.: Using the OMI aerosol index and absorption
742 aerosol optical depth to evaluate the NASA MERRA Aerosol Reanalysis,
743 *Atmospheric Chemistry and Physics*, 15(10), 5743-5760, 2015.
- 744 Chen, X., Zuo, H., Zhang, Z., Cao, X., Duan, J., Zhu, C., Zhang, Z., Wang, J.: Full-
745 coverage 250 m monthly aerosol optical depth dataset (2000–2019) amended with
746 environmental covariates by an ensemble machine learning model over arid and
747 semi-arid areas, NW China, *Earth System Science Data*, 14(12), 5233-5252, 2022.
- 748 Chen, S., Huang, J., Zhao, C., Qian, Y., Leung, L. R., Yang, B.: Modeling the transport
749 and radiative forcing of Taklimakan dust over the Tibetan Plateau: A case study in
750 the summer of 2006, *Journal of Geophysical Research: Atmospheres*, 118(2), 797-
751 812, 2013.
- 752 Chen, S., Zhang, R., Mao, R., Zhang, Y., Chen, Y., Ji, Z., Gong, Y., Guan, Y.: Sources,
753 characteristics and climate impact of light-absorbing aerosols over the Tibetan
754 Plateau, *Earth-Science Reviews*, 232, 104111, 2022.
- 755 Carrió, G. G., van Den Heever, S. C., Cotton, W. R.: Impacts of nucleating aerosol on
756 anvil-cirrus clouds: A modeling study, *Atmospheric research*, 84(2), 111-131, 2007.
- 757 Guan, H., Esswein, R., Lopez, J., Bergstrom, R., Warnock, A., Follette-Cook, M., Iraci,
758 L. T.: A multi-decadal history of biomass burning plume heights identified using
759 aerosol index measurements, *Atmospheric Chemistry and Physics*, 10(14), 6461-
760 6469, 2010.
- 761 Guan, H., Chatfield, R. B., Freitas, S. R., Bergstrom, R. W., Longo, K. M.: Modeling
762 the effect of plume-rise on the transport of carbon monoxide over Africa with
763 NCAR CAM, *Atmos. Chem. Phys.*, 8, 6801–6812, doi:10.5194/acp-8-6801-2008,
764 2008.
- 765 Goldberg, D. L., Gupta, P., Wang, K., Jena, C., Zhang, Y., Lu, Z., Streets, D. G.: Using



- 766 gap-filled MAIAC AOD and WRF-Chem to estimate daily PM_{2.5} concentrations
767 at 1 km resolution in the Eastern United States, *Atmos. Environ.*, 199, 443–452,
768 <https://doi.org/10.1016/j.atmosenv.2018.11.049>, 2019.
- 769 Giles, D. M., Sinyuk, A., Sorokin, M. G., Schafer, J. S., Smirnov, A., Slutsker, I., Eck,
770 T. F., Holben, B. N., Lewis, J. R., Campbell, J. R., Welton, E. J., Korkin, S. V., and
771 Lyapustin, A. I.: Advancements in the Aerosol Robotic Network (AERONET)
772 Version 3 database – automated near-real-time quality control algorithm with
773 improved cloud screening for Sun photometer aerosol optical depth (AOD)
774 measurements, *Atmos. Meas. Tech.*, 12, 169–209, [https://doi.org/10.5194/amt-12-](https://doi.org/10.5194/amt-12-169-2019)
775 169-2019, 2019.
- 776 Guan, H., Esswein, R., Lopez, J., Bergstrom, R., Warnock, A., Follette-Cook, M.,
777 Fromm, M., Iraci, L. T.: A multi-decadal history of biomass burning plume heights
778 identified using aerosol index measurements, *Atmospheric Chemistry and Physics*,
779 10(14), 6461-6469, 2010.
- 780 Hsu, N. C., Si-Chee, T., King, M. D., Herman, J. R.: Aerosol properties over bright-
781 reflecting source regions, *IEEE Trans. Geosci. Rem. Sens.*, 42, 557–569, 2004.
- 782 Hammer, M. S., Martin, R. V., Li, C., Torres, O., Manning, M., Boys, B. L.: Insight into
783 global trends in aerosol composition from 2005 to 2015 inferred from the OMI
784 Ultraviolet Aerosol Index, *Atmospheric Chemistry and Physics*, 18(11), 8097-
785 8112, 2018.
- 786 Hu, Q., Wang, H., Goloub, P., Li, Z., Veselovskii, I., Podvin, T., Li, K., Korenskiy, M.:
787 The characterization of Taklamakan dust properties using a multiwavelength
788 Raman polarization lidar in Kashi, China, *Atmospheric Chemistry and Physics*,
789 20(22), 13817-13834, 2020.
- 790 Hu, Y., S. Rodier, K. Xu, W. Sun, J. Huang, B. Lin, P. Zhai, and D. Josset.: Occurrence, liquid
791 water content, and fraction of supercooled water clouds from combined
792 CALIOP/IIR/MODIS measurements, *J. Geophys. Res.*, 115, D00H34,
793 doi:10.1029/2009JD012384, 2010.
- 794 Huang, L., Jiang, J. H., Tackett, J. L., Su, H., Fu, R.: Seasonal and diurnal variations of
795 aerosol extinction profile and type distribution from CALIPSO 5-year



796 observations, *Journal of Geophysical Research: Atmospheres*, 118(10), 4572-4596,
797 2013.

798 Huang, J., Minnis, P., Chen, B., Huang, Z., Liu, Z., Zhao, Q., Yi, Y., Ayers, J. K.: Long-
799 range transport and vertical structure of Asian dust from CALIPSO and surface
800 measurements during PACDEX, *Journal of Geophysical Research: Atmospheres*,
801 113(D23), 2008.

802 Immerzeel, W., Van Beek, L., Bierkens, M.: Climate change will affect the Asian water
803 towers, *Science*, 328 (5984), 1382-1385, 2010.

804 IPCC: Climate Change 2013: The Physical Science Basis. Contribution of Working
805 Group I to the Fifth Assessment Report of the Intergovernmental Panel on Climate
806 Change, edited by: Stocker, T. F., Qin, D., Plattner, G.-K., Tignor, M., Allen, S. K.,
807 Boschung, J., Nauels, A., Xia, Y., Bex, V., and Midgley, P. M., Cambridge
808 University Press, Cambridge, United Kingdom and New York, NY, USA, 1535 pp.,
809 2013.

810 IPCC, 2021: Climate Change 2021: The Physical Science Basis. Contribution of
811 Working Group I to the Sixth Assessment Report of the Intergovernmental Panel
812 on Climate Change, edited by: Masson-Delmotte, V., P. Zhai, A. Pirani, S.L.
813 Connors, C. Péan, S. Berger, N. Caud, Y. Chen, L. Goldfarb, M.I. Gomis, M.
814 Huang, K. Leitzell, E. Lonnoy, J.B.R. Matthews, T.K. Maycock, T. Waterfield, O.
815 Yelekçi, R. Yu, and B. Zhou (eds.]. Cambridge University Press, Cambridge,
816 United Kingdom and New York, NY, USA, In press, doi:10.1017/9781009157896.

817 Iglewicz, B. and Hoaglin, D.: How to Detect and Handle Outliers, ASQC basic
818 references in quality control, ASQC Quality Press, Milwaukee, 1993.

819 Kovilakam, M., Thomason, L. W., Ernest, N., Rieger, L., Bourassa, A., Millán, L.: The
820 global space-based stratospheric aerosol climatology (version 2.0): 1979–2018,
821 *Earth System Science Data*, 12(4), 2607-2634, 2020.

822 Kahn, R. A., Gaitley, B. J., Garay, M. J., Diner, D. J., Eck, T. F., Smirnov, A., Holben,
823 B. N.: Multiangle Imaging Spectroradiometer global aerosol product assessment
824 by comparison with the Aerosol Robotic Network, *J. Geophys. Res.-Atmos.*, 115,
825 D23209, doi:10.1029/2010jd014601, 2010.



- 826 Kojima, T., Buseck, P. R., Wilson, J. C., Reeves, J. M., Mahoney, M. J.: Aerosol
827 particles from tropical convective systems: Cloud tops and cirrus anvils, *Journal*
828 *of Geophysical Research: Atmospheres*, 109(D12), 2004.
- 829 Kim, M.H., Omar, A.H., Tackett, J.L., Vaughan, M.A., Winker, D.M., Trepte, C.R., Hu,
830 Y., Liu, Z., Poole, L.R., Pitts, M.C., Kar, J., Magill, B.E.: The CALIPSO Version 4
831 Automated Aerosol Classification and Lidar Ratio Selection Algorithm,
832 *Atmospheric Measurement Techniques*, 11(11):6107-6135, 2018.
- 833 Liu, Y., Huang, J., Wang, T., Li, J., Yan, H., He, Y.: Aerosol-cloud interactions over the
834 Tibetan Plateau: An overview, *Earth-Science Reviews*, 104216, 2022.
- 835 Liu, Y., Li, Y., Huang, J., Zhu, Q., Wang, S.: Attribution of the Tibetan Plateau to
836 northern drought, *National Science Review*, 7(3), 489-492, 2020.
- 837 Liu, Y., Hua, S., Jia, R., Huang, J.: Effect of aerosols on the ice cloud properties over
838 the Tibetan Plateau, *Journal of Geophysical Research: Atmospheres*, 124(16),
839 9594-9608, 2019.
- 840 Luo, H., Yanai, M.: The large-scale circulation and heat sources over the Tibetan
841 Plateau and surrounding areas during the early summer of 1979, Part II: Heat and
842 moisture budgets, *Mon. Wea. Rev.*, 112, 966–989, 1984.
- 843 Liou, K.: Influence of cirrus clouds on weather and climate processes: a global
844 perspective, *Mon. Weather Rev.*, 114, 1167–1199, 1986.
- 845 Liu, Z., Kar, J., Zeng, S., Tackett, J., Vaughan, M., Avery, M., Pelon, J., Getzewich, B.,
846 Lee, K.P., Magill, B., Omar, A., Lucker, P., Trepte, C., Winker, D.: Discriminating
847 between clouds and aerosols in the caliop version 4.1 data products, *Atmos. Meas.*
848 *Tech.*, 12, 703–734, 2019.
- 849 Liu, D., Z. Wang, Z. Liu, D. Winker, C. Trepte.: A height resolved global view of dust
850 aerosols from the first year CALIPSO lidar measurements, *J. Geophys. Res.*, 113,
851 D16214, doi:10.1029/2007JD009776, 2008.
- 852 Liu, Z., Liu, D., Huang, J., Vaughan, M., Uno, I., Sugimoto, N., Kittaka, C., Trepte, C.,
853 Wang, Z., Hostetler, C., Winker, D.: Airborne dust distributions over the Tibetan
854 Plateau and surrounding areas derived from the first year of CALIPSO lidar
855 observations, *Atmospheric Chemistry and Physics*, 8(16), 5045-5060, 2008.



- 856 Liu, P. F., C. S. Zhao, Q. Zhang, Z. Z. Deng, M. Y. Huang, X. C. Ma, X. X. Tie.: Aircraft
857 study of aerosol vertical distributions over Beijing and their optical properties,
858 *Tellus, Ser. B*, 61(5), 756–767, doi:10.1111/j.1600-0889.2009.00440.x, 2009.
- 859 Molnar,P., Boos,W., Battisti, D.: Orographic controls on climate and paleoclimate of
860 Asia: thermal and mechanical roles for the Tibetan Plateau, *Annu. Rev. Earth*
861 *Pl.Sc.*, 38 (1), 77-102, 2010.
- 862 Matsuki, A., Iwasaka, Y., Osada, K., Matsunaga, K., Kido, M., Inomata, Y., Trochkin,
863 D., Nishita, C., Nezuka, T., Sakai,T., Zhang,D., Kwon, S. A.: Seasonal dependence
864 of the long - range transport and vertical distribution of free tropospheric aerosols
865 over east Asia: On the basis of aircraft and lidar measurements and isentropic
866 trajectory analysis, *Journal of Geophysical Research: Atmospheres*, 108(D23),
867 2003.
- 868 Nieberding, F., Wille, C., Fratini, G., Asmussen, M. O., Wang, Y., Ma, Y., Sachs, T.: A
869 long-term (2005–2019) eddy covariance data set of CO₂ and H₂O fluxes from the
870 Tibetan alpine steppe, *Earth System Science Data*, 12(4), 2705-2724, 2020.
- 871 Nakajima, T., Higurashi, A., Kawamoto, K., Penner, J. E.: A possible correlation
872 between satellite - derived cloud and aerosol microphysical parameters,
873 *Geophysical Research Letters*, 28 (7), 1171 - 1174,
874 <https://doi.org/10.1029/2000GL012186>, 2001.
- 875 Pan, H., Huo, W., Wang, M., Zhang, J., Meng, L., Kumar, K. R., Devi, N. L.: Insight
876 into the climatology of different sand-dust aerosol types over the Taklimakan
877 Desert based on the observations from radiosonde and A-train satellites,
878 *Atmospheric Environment*, 238, 117705, 2020.
- 879 Qiu, J.: China: The third pole, *Nature*, 454, 393-396, <https://doi.org/10.1038/454393a>,
880 2008.
- 881 Rossow, W., Schiffer, R.: Advances in understanding clouds from ISCCP, *Bull. Am.*
882 *Meteorol. Soc.*, 80, 2261 - 2287, 1999.
- 883 Rieger, L. A., Bourassa, A. E., Degenstein, D. A.: Merging the OSIRIS and SAGE II
884 stratospheric aerosol records, *J. Geophys. Res. Atmos.*, 120, 8890–8904,
885 <https://doi.org/10.1002/2015JD023133>, 2015.



- 886 Rieger, L. A., Zawada, D. J., Bourassa, A. E., Degenstein, D. A.: A Multiwavelength
887 Retrieval Approach for Improved OSIRIS Aerosol Extinction Retrievals, *J.*
888 *Geophys. Res.-Atmos.*, 124, 7286–7307, <https://doi.org/10.1029/2018JD029897>,
889 2019.
- 890 Seifert, P., Ansmann, A., Müller, D., Wandinger, U., Althausen, D., Heymsfield, A. J.,
891 Massie, S.T., Schmitt, C.: Cirrus optical properties observed with lidar, radiosonde,
892 and satellite over the tropical Indian Ocean during the aerosol-polluted northeast
893 and clean maritime southwest monsoon, *Journal of Geophysical Research:*
894 *Atmospheres*, 112(D17), 2007.
- 895 Sasano, Y.: Tropospheric aerosol extinction coefficient profiles derived from scanning
896 lidar measurements over Tsukuba, Japan from 1990 to 1993, *Appl. Opt.*, 35(24),
897 4941–4952, 1996.
- 898 Thomason, L. W. and Vernier, J.-P.: Improved SAGE II cloud/aerosol categorization
899 and observations of the Asian tropopause aerosol layer: 1989–2005, *Atmos. Chem.*
900 *Phys.*, 13, 4605–4616, <https://doi.org/10.5194/acp-13-4605-2013>, 2013.
- 901 Twomey, S.A.: The influence of pollution on the shortwave albedo of clouds, *J. Atmos.*
902 *Sci.*, 34 (7), 1149 – 1154, 1977.
- 903 Torres, O., Bhartia, P. K., Herman, J. R., Ahmad, Z., and Gleason, J.: Derivation of
904 aerosol properties from satellite measurements of backscattered ultraviolet
905 radiation: Theoretical basis, *J. Geophys. Res.*, 103, 17099–17110,
906 doi:10.1029/98JD00900, 1998.
- 907 Torres, O., Tanskanen, A., Veihelmann, B., Ahn, C., Braak, R., Bhartia, P. K., Veefkind,
908 P., Levelt, P.: Aerosols and surface UV products from Ozone Monitoring
909 Instrument observations: An overview, *J. Geophys. Res.*, 112, D24S47,
910 doi:10.1029/2007JD008809, 2007.
- 911 Vernier, J. P., Fairlie, T. D., Natarajan, M., Wienhold, F. G., Bian, J., Martinsson, B. G.,
912 Crumeyrolle, S., Thomason, L.W., Bedka, K. M.: Increase in upper tropospheric
913 and lower stratospheric aerosol levels and its potential connection with Asian
914 pollution, *Journal of Geophysical Research: Atmospheres*, 120(4), 1608-1619,
915 2015.



- 916 Wan, B., Gao, Z., Chen, F., Lu, C.: Impact of Tibetan Plateau surface heating on
917 persistent extreme precipitation events in Southeastern China, *Mon. Weather Rev.*,
918 145 (9), 3485–3505, 2017.
- 919 Winker, D. M., Vaughan, M. A., Omar, A., Hu, Y., Powell, K. A., Liu, Z., Hunt, W. H.,
920 and Young, S. A.: Overview of the CALIPSO mission and CALIOP data
921 processing algorithms, *J. Atm. Ocean. Techn.*, 26, 2310–2323, 2009.
- 922 Winker, D.M., Hunt, W.H., McGill, M.J.: Initial performance assessment of CALIOP,
923 *Geophys. Res. Lett.*, 34, L19803, <https://doi.org/10.1029/2007GL030135>, 2007.
- 924 Wu, G., Zhang, Y.: Tibetan Plateau forcing and the timing of the monsoon onset over
925 South Asia and the South China Sea, *Mon. Wea. Rev.*, 126, 913-927, 1998.
- 926 Wu, G., Liu, Y., Zhang, Q., Duan, A., Wang, T., Wan, R., Liu, X., Li, W., Wang, Z.,
927 Liang, X.: The influence of mechanical and thermal forcing by the Tibetan Plateau
928 on Asian climate, *J. Hydro. Meteor. Spec. Sect.*, 8 (4), 770-789, 2007.
- 929 Wu, G., Liu, Y., Dong, B., Liang, X., Duan, A., Bao, Q., Yu, J.: Revisiting Asian
930 monsoon formation and change associated with Tibetan Plateau forcing: I.
931 Formation, *Climate dynamics*, 39, 1169-1181, 2012.
- 932 Wu, G., Duan, A., Liu, Y., Mao, J., Ren, R., Bao, Q., He, B., Liu, B., Hu, W.: Tibetan
933 Plateau climate dynamics: recent research progress and outlook, *Natl. Sci. Rev.*, 2
934 (1), 100-116, 2015.
- 935 Wei, X., Bai, K., Chang, N.-B., Gao, W.: Multi-source hierarchical data fusion for high-
936 resolution AOD mapping in a forest fire event, *International Journal of Applied
937 Earth Observation and Geoinformation*, 102, 102366,
938 <https://doi.org/10.1016/j.jag.2021.102366>, 2021.
- 939 Xu, X., Lu, C., Shi, X., Gao, S.: World water tower: an atmospheric perspective,
940 *Geophys. Res. Lett.*, 35 (20), 2008.
- 941 Xu, C., Ma, Y. M., You, C., Zhu, Z. K.: The regional distribution characteristics of
942 aerosol optical depth over the Tibetan Plateau, *Atmospheric Chemistry and
943 Physics*, 15(20), 12065-12078, 2015.
- 944 Yanai, M., Li, C., Song, Z.: Seasonal heating of the Tibetan Plateau and its effects on
945 the evolution of the Asian summer monsoon, *J. Meteor. Soc. Japan* 70, 319-



946 351,1992.

947 Zhang, S., Huang, Z., Li, M., Shen, X., Wang, Y., Dong, Q., Bi J., Zhang J., Li W., Li

948 Z., Song, X.: Vertical structure of dust aerosols observed by a ground-based raman

949 lidar with polarization capabilities in the center of the Taklimakan desert, Remote

950 Sensing, 14(10), 2461, 2022.

951 Zhang, S., Huang, Z., Alam, K., Li, M., Dong, Q., Wang, Y., Shen, X., Bi, J., Zhang, J.,

952 Li, W., Li, Z., Wang, W., Cui, Z., Song, X.: Derived Profiles of CCN and INP

953 Number Concentrations in the Taklimakan Desert via Combined Polarization

954 Lidar, Sun-Photometer, and Radiosonde Observations, Remote Sensing, 1–20.

955 <https://doi.org/10.3390/rs15051216>, 2023.

956 Zhou, J., G. Yu, C. Jin, F. Qi, D. Liu, H. Hu, Z. Gong, G. Shi, T. Nakajima, T. Takamura.:

957 Lidar observations of Asian dust over Hefei, China in Spring 2000, J. Geophys.

958 Res., 107(D15), 4252, doi:10.1029/2002.2001JD000802, 2002.

959

960

961